ATLAS CONF Note

ATLAS-CONF-2018-005

4th April 2018

Search for dark matter in events with a hadronically decaying vector boson and missing transverse momentum in pp collisions at $\sqrt{s} = 13$ TeV with the ATLAS detector

The ATLAS Collaboration

The search for dark matter (DM) particles produced in association with a hadronically decaying vector boson is performed with 36.1 fb^{-1} of pp collision data at a centre-of-mass energy of $\sqrt{s} = 13$ TeV recorded by the ATLAS detector at the Large Hadron Collider. This analysis improves on the previous searches for processes with hadronic decays of W and Z bosons in association with large missing transverse momentum (mono-W/Z searches) due to the larger dataset and further optimization of the event selection and signal region definitions. In addition to the mono-W/Z search, yet unexplored hypothesis of a new vector boson Z' produced in association with dark matter is considered (mono-Z' search). No significant excess over the Standard Model prediction is observed. The results of the mono-W/Z search are interpreted in terms of limits on the invisible Higgs boson decays into dark matter particles, constraints on the parameter space of the simplified vector-mediator model and generic upper limits on the visible cross sections for the W/Z+DM production. The results of the mono-Z' search are shown in the frame of several simplified-model scenarios involving the DM production in association with the Z' boson.

ATLAS-CONF-2018-005
06 April 2018

1 Introduction

Numerous cosmological observations indicate that a large part of the mass of the universe is composed of the dark matter (DM), yet its exact, possibly particle nature and the connection to the Standard Model (SM) of particle physics remain unknown. Discovery of DM particles and understanding of their interactions with SM particles is one of the greatest quests in particle physics and cosmology today, exploiting several different experimental approaches. Indirect detection experiments are searching for signs of DM annihilation or decays in outer space and direct detection experiments are sensitive to low-energy recoils of nuclei induced by interactions with DM particles from the galactic halo. The interpretation of these searches is subject to astrophysical uncertainties on DM abundance and composition. Searches at particle colliders, irrelevant for these uncertainties, are complementary if DM candidates can be produced in particle collisions. Weakly interacting massive particles (WIMPs), one of the leading DM candidates, could be produced in proton–proton (pp) collisions at the Large Hadron Collider (LHC) and detected by measuring the momentum imbalance associated with the recoiling SM particles.

A typical DM signature which can be detected by the LHC experiments is a large overall missing transverse momentum $E_{\mathrm{T}}^{\mathrm{miss}}$ associated with a pair of DM particles which are recoiling against one or more SM particles. Several searches for such signatures have been performed with LHC pp collision data at centre-of-mass energies of 7, 8 and 13 TeV. No deviations from SM predictions have been observed so far and limits are set on various DM particle models. Measurements probing the DM production in association with a hadronically decaying W or Z boson [1–4] are accompanied by dedicated searches for the so-called invisible decays of the SM-like Higgs boson into a pair of DM particles, targeting the Higgs boson production in association with a hadronically decaying vector boson [5–7]. In the SM, the invisible Higgs boson decays occur through the $H \to ZZ^{\star} \to \nu\nu\nu\nu$ process with a branching ratio $\mathcal{B}^{\mathrm{SM}}_{H\to\mathrm{inv.}}$ of 1.06×10^{-3} for a Higgs boson mass $m_H = 125$ GeV [8]. Some extensions of the SM allow for invisible decays of the Higgs boson into DM or neutral long-lived massive particles [9–13] with a significantly larger branching ratio $\mathcal{B}_{H\to\mathrm{inv.}}$. Presently the most stringent upper limit on $\mathcal{B}_{H\to\mathrm{inv.}}$ is about 23% at 95% confidence level (CL) for $m_H = 125$ GeV, obtained from a combination of direct searches and indirect constraints of Higgs bosons coupling measurements [5, 14].

In this note, the search for DM particles produced in association with a hadronically decaying W or Z boson (mono-W/Z search) is performed for specific DM models, including the DM production via invisible Higgs boson decays, using LHC pp collision data at a centre-of-mass energy of 13 TeV collected by the ATLAS experiment in 2015 and 2016, corresponding to a total integrated luminosity of 36.1 fb^{-1}. The results are also expressed in terms of upper limits on visible cross sections, allowing to reinterpret the search results in alternative models. In addition to the mono-W/Z search, the yet unexplored hypothesis of the DM production in association with a potentially new vector boson Z' [15] has been studied using the same collision data (mono-Z' search). Compared to the analysis presented in Ref. [1], event selection and definition of the signal regions is further optimized, including new signal regions based on the tagging of jets from heavy-flavor hadrons and on jet topologies. Event topologies with two well-separated jets from the vector boson decay are studied (referred to as *resolved topology*), as well as the topologies with one large-radius jet from a highly boosted vector boson (referred to as *merged topology*).

The note is organized as follows. A brief introduction of the ATLAS detector is given in Section 2. The signal models are introduced in Section 3, while the simulated samples of signal and background processes are described in Section 4. The algorithms for the reconstruction and identification of final state particles are summarized in Section 5. Section 6 describes the criteria for the selection of candidate signal events. The background contributions are estimated with the help of dedicated control regions in data, as

described in Section 7. The experimental and theoretical systematic uncertainties (Section 8) are taken into account for the statistical interpretation of data, with the results presented in Section 9. Concluding remarks are given in Section 10.

2 ATLAS detector

The ATLAS detector [16] is a general-purpose detector with forward-backward symmetric cylindrical geometry.[1] It consists of an inner tracking detector (ID), electromagnetic (EM) and hadronic calorimeters and a muon spectrometer (MS) surrounding the interaction point. A new innermost silicon pixel layer [17, 18] was added to the ID before the start of data taking in 2015. The inner tracking system is immersed in a 2 T axial magnetic field, while toroidal magnets in the MS provide a field integral ranging from 2 Tm to 6 Tm across most of the MS. The electromagnetic calorimeter is a lead/liquid-argon (LAr) sampling calorimeter with an accordion geometry covering the pseudorapidity range $|\eta| < 3.2$. Downstream of the EM calorimeter, hadronic calorimetry is provided by a steel/scintillator-tile calorimeter in the range $|\eta| < 1.7$ and two copper/LAr calorimeters spanning $1.5 < |\eta| < 3.2$. The calorimeter coverage is extended to $|\eta| < 4.9$ by the copper/LAr and tungsten/LAr forward calorimeters providing both the electromagnetic and hadronic energy measurements. The data are collected with a two-level trigger system. The first-level trigger selects events based on a custom-made hardware and uses information from muon detectors and calorimeters with coarse granularity. The second-level trigger is based on software algorithms similar to those applied for the offline event reconstruction and uses the full detector granularity.

3 Signal models

Two signal models are used to describe the DM production in the mono-W/Z final state. The first is a *simplified vector-mediator model*, illustrated by a Feynman diagram in Figure 1(a), in which a pair of Dirac DM particles is produced via an s-channel exchange of a vector mediator (Z') [19, 20]. There are four free parameters in this model: the DM and the mediator mass (m_χ and $m_{Z'}$, respectively), as well as the mediator couplings to the SM and DM particles (g_{SM} and g_{DM}, respectively). The minimal total mediator decay width is assumed, allowing only for vector mediator decays into DM or quarks. Its value is determined by the choice of the coupling values g_{SM} and g_{DM} [20] and it is much smaller than the mediator mass. The second is a model with *invisible Higgs boson decays* in which a SM-like Higgs boson H produced in different SM Higgs boson production processes decays into a pair of DM particles which escape the detection. The production process with the final state closest to the mono-W/Z signature is the associated production with a hadronically decaying W or Z boson (VH production, see Figure 1(b)). The WH and ZH signals are predominantly produced via quark-antiquark annihilation ($q\bar{q} \to VH$), with an additional ZH contribution from the gluon-gluon fusion ($gg \to ZH$). The Higgs boson production via gluon-gluon fusion (ggH) or vector boson fusion (VBF) followed by the Higgs boson decay into DM particles can also lead to events with large $E_{\text{T}}^{\text{miss}}$ and two or more jets. Especially the ggH signal has a

[1] The ATLAS experiment uses a right-handed coordinate system with its origin at the nominal interaction point (IP) in the center of the detector and the z-axis along the beam pipe. The x-axis points from the IP to the center of the LHC ring, and the y-axis points upward. Cylindrical coordinates (r, ϕ) are used in the transverse plane, ϕ being the azimuthal angle around the z-axis. The pseudorapidity is defined in terms of the polar angle θ as $\eta = -\ln\tan(\theta/2)$. Transverse momenta are computed from the three-momenta, $\boldsymbol{p}$, as $p_{\text{T}} = |\boldsymbol{p}| \sin\theta$.

contribution comparable to or even stronger than the VH process, since its cross section is about 20 times larger and the jets originating from the initial state radiation are more central than in the VBF process. The free parameter of this model is the branching ratio $\mathcal{B}_{H\to\text{inv.}}$. The cross sections for the different Higgs boson production modes are taken to be given by the SM predictions.

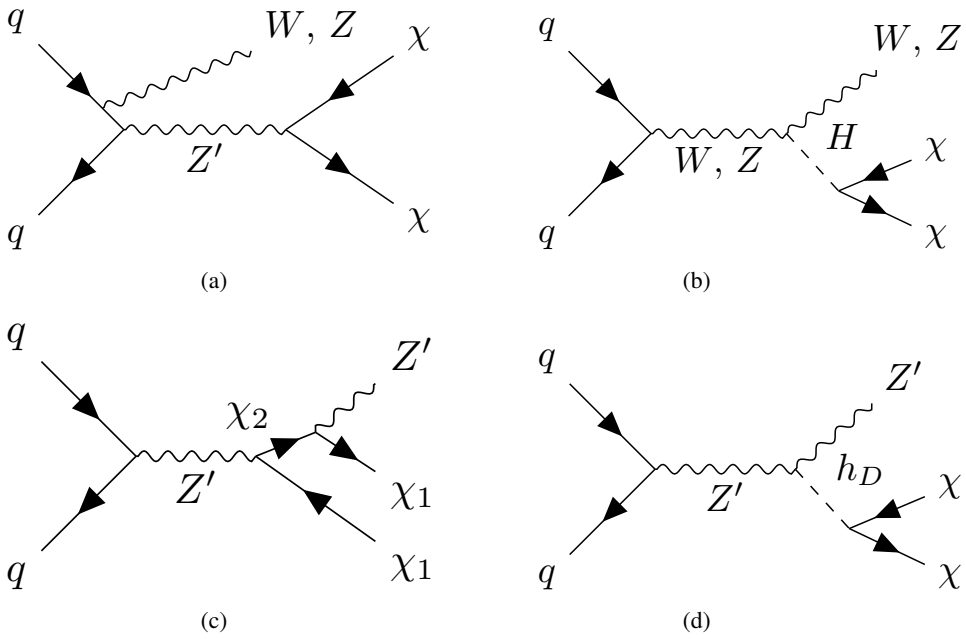

Figure 1: Examples of dark matter particle (χ) pair-production in association with (a) a W or Z boson in a simplified model with a vector mediator Z' between the dark sector and the SM [19] and (b) via decay of the SM-like Higgs boson produced in association with the vector boson [9–13] or in association with a final-state Z' boson via (c) an additional heavy dark-sector fermion (χ_2) [15] or (d) via a dark-sector Higgs boson (h_D) [15].

Two signal models describe DM production in the mono-Z' final state [15]. Both models contain the Z' boson in the final state, which is allowed to decay only hadronically, i.e. $Z' \to q\bar{q}$ with all possible quark flavors, except for the $t\bar{t}$ decay channel. In the first model, the so-called *dark-fermion model*, the intermediate Z' boson couples to a heavier dark-sector fermion χ_2 as well as the lighter DM candidate fermion χ_1, see Figure 1(c). The mass m_{χ_2} of the heavy fermion χ_2 is a free parameter of the model, in addition to the DM candidate mass m_{χ_1}, mediator mass $m_{Z'}$, as well as the Z' couplings to $\chi_1\chi_2$ (g_{DM}) and to all SM particles (g_{SM}). The total Z' and χ_2 decay widths are determined by the choice of the mass and coupling parameter values, assuming that the only allowed decay modes are $\chi_2 \to Z'\chi_1$, $Z' \to q\bar{q}$ and $Z' \to \chi_2\chi_1$. Under these assumptions the decay widths are small compared to the experimental di-jet and large-radius jet mass resolutions. In the second, so-called *dark-Higgs model*, a dark-sector Higgs boson which decays to $\chi\chi$ pair is radiated from the Z' boson as illustrated in Figure 1(d). The mass m_{h_D} and the width Γ_{h_D} of the dark Higgs boson are free parameters of the model, in addition to m_χ, $m_{Z'}$, g_{SM} and g_{DM}. The latter is defined as the coupling of the dark Higgs boson h_D to the vector boson Z'. Similarly as for the dark-fermion model, the total decay widths of the Z' and h_D bosons are determined by the values of the mass and coupling parameters, assuming that the Z' boson can only decay into quarks or radiate an h_D boson. The dark Higgs boson is assumed to decay only into $\chi\chi$ or $Z'Z'^{(*)}$. The latter decay mode is suppressed for $m_{h_D} < 2m_{Z'}$, which is the case for the parameter space considered in this note.

4 Simulated signal and background samples

All signal and background processes from hard-scatter pp collisions are modeled by simulating the detector response to particles produced with Monte Carlo (MC) event generators. The interaction of generated particles with the detector material is modeled with the GEANT4 [21] package and the same particle reconstruction algorithms are employed in simulation as in the data. Additional pp interactions in the same and nearby bunch crossings (pile-up) are taken into account in simulation. The pile-up events were generated using PYTHIA 8.186 [22] with the A2 set of tuned parameters [23] and the MSTW2008LO set of parton distribution functions (PDF) [24]. The simulation samples were weighted to reproduce the observed distribution of the mean number of interactions per bunch crossing in the data.

The mono-W/Z signal processes within the simplified Z' vector-mediator model, as well as all mono-Z' signal processes are modeled at the leading-order (LO) accuracy with the MadGraph5_aMC@NLO v2.2.2 generator [25] interfaced respectively to the PYTHIA 8.186 and PYTHIA 8.210 parton shower models. The A14 set of tuned parameters [26] is used together with the NNPDF23lo PDF set [27] for these signal samples. The mono-W/Z signal samples within the simplified vector-mediator model are generated in a grid of mediator and DM particle masses, with coupling values set to $g_{\mathrm{SM}} = 0.25$ and $g_{\mathrm{DM}} = 1$ following the 'V1' scenario from Ref. [28]. The mediator mass $m_{Z'}$ and the DM particle mass m_{χ} range from 10 GeV to 10 TeV and from 1 GeV to 1 TeV, respectively. Two samples with $m_{\chi} = 1$ GeV have been used to evaluate the impact of theory uncertainties on the signal, one with a mediator mass of 300 GeV and the other with 600 GeV. The mono-Z' samples are simulated for mediator masses between 50 GeV and 500 GeV, with the g_{DM} coupling value set to $g_{\mathrm{DM}} = 1$. Following the current experimental constraints from dijet resonance searches [29–32], in particular those for the mediator mass range below about 500 GeV studied in this analysis, the g_{SM} coupling value is set to 0.1. For this choice of the couplings, the width of the Z' boson is negligible compared to the experimental resolution, allowing to set limits on the coupling product $g_{\mathrm{SM}} \cdot g_{\mathrm{DM}}$. For each choice of $m_{Z'}$, two signal samples are simulated in both mono-Z' models, each with a different choice of masses m_{χ_2} and m_{h_D} of intermediate dark-sector particles as summarized in Table 1. Out of the two samples for a given m'_Z value, the one with a lower (higher) mass of the intermediate dark-sector particle is referred to as the 'light dark sector' ('heavy dark sector') scenario. The mass m_{χ} in the dark-Higgs model is set to 5 GeV, since it can be assumed that the kinematic properties are determined by the masses $m_{Z'}$ and m_{h_D} unless the mass m_{χ} is too large.

Table 1: Particle mass settings in the simulated mono-Z' samples for a given mediator mass $m_{Z'}$.

Scenario	Dark-fermion model	Dark-Higgs model
Light dark sector	$m_{\chi_1} = 5$ GeV $m_{\chi_2} = m_{\chi_1} + m_{Z'} + 25$ GeV	$m_{\chi} = 5$ GeV $m_{h_D} = \begin{cases} m_{Z'} & , m_{Z'} < 125 \text{ GeV} \\ 125 \text{ GeV} & , m_{Z'} > 125 \text{ GeV} \end{cases}$
Heavy dark sector	$m_{\chi_1} = m_{Z'}/2$ $m_{\chi_2} = 2m_{Z'}$	$m_{\chi} = 5$ GeV $m_{h_D} = \begin{cases} 125 \text{ GeV} & , m_{Z'} < 125 \text{ GeV} \\ m_{Z'} & , m_{Z'} > 125 \text{ GeV} \end{cases}$

Processes in the mono-W/Z final state involving invisible Higgs boson decays originate from the VH, ggH and VBF SM Higgs boson production mechanisms and are all generated with the POWHEG-BOX v2

generator interfaced to Pythia 8.212 for the parton shower modeling. The detailed description of all generated production processes together with the corresponding cross section calculations can be found in Refs. [33, 34]. The Higgs boson mass in these samples is set to $m_H = 125$ GeV and the Higgs boson is decayed through the $H \to ZZ^* \to \nu\nu\nu\nu$ process to emulate the decay of the Higgs boson into invisible particles. The branching ratio for the Higgs boson decay is set to $\mathcal{B}_{H\to\text{inv.}} = 100\%$.

The major sources of background are the production of top-quark pairs ($t\bar{t}$) and the production of W and Z bosons in association with jets (V+jets, where $V \equiv W$ or Z). The event rates and the shape of the final discriminant observables in these processes are further constrained with data from dedicated control regions (see Section 7). Other small background contributions include diboson (WW, WZ and ZZ) and single top-quark production. Their contribution is estimated from simulation.

Events containing leptonically decaying W or Z bosons with associated jets are simulated using the Sherpa 2.2.1 generator [35], with matrix elements calculated for up to two partons at next-to-leading order (NLO) and four partons at LO using Comix [36] and OpenLoops [37] and merged with the Sherpa parton shower [38] using the ME+PS@NLO prescription [39]. The NNPDF3.0 next-to-next-to-leading (NNLO) PDF set is used in conjunction with dedicated parton shower tuning developed by the Sherpa authors. The inclusive cross section is calculated up to NNLO order in QCD [40].

For the generation of $t\bar{t}$ events, Powheg-Box v2 [41–43] is used with the CT10 PDF set in the matrix element calculations. Electroweak t-channel, s-channel and Wt-channel single top-quark events are generated with Powheg-Box v1. This event generator uses the four-flavor scheme for the NLO matrix element calculations together with the fixed four-flavor PDF set CT10f4. For all top-quark processes, top-quark spin correlations are preserved (for t-channel top quark production, top quarks are decayed using MadSpin [44]). The parton shower, hadronization, and the underlying event are simulated using Pythia 6.428 [45] with the CTEQ6L1 PDF set [46] and the corresponding Perugia 2012 set of tuned parameters [47]. The top-quark mass is set to 172.5 GeV. The EvtGen 1.2.0 program [48] is used for the properties of b- and c-hadron decays. The inclusive $t\bar{t}$ cross section is calculated up to NNLO with soft gluon resummation at the next-to-next-to-leading-logarithm (NNLL) accuracy [49]. Single top-quark production cross-sections are calculated at NLO accuracy [50–53].

Diboson events with one of the bosons decaying hadronically and the other leptonically are generated with the Sherpa 2.1.1 event generator. They are calculated for up to one (ZZ) or zero (WW, WZ) additional partons at NLO and up to three additional partons at LO using Comix and OpenLoops, and merged with the Sherpa parton shower according to the ME+PS@NLO prescription. The CT10 PDF set is used in conjunction with dedicated parton shower tuning developed by the Sherpa authors. The event generator cross sections at NLO are used in this case. In addition, the Sherpa diboson sample cross section is scaled down to account for its use of α=1/129 rather than 1/132 corresponding to the use of current PDG parameters as input to the G_μ scheme [54].

5 Object reconstruction and identification

The selection of mono-W/Z and mono-Z' candidate signal events and events in dedicated one-muon and two-lepton (electron or muon) control regions relies on the reconstruction and identification of jets, electrons and muons, as well as on the reconstruction of the missing transverse momentum. These will be described in the following.

Three types of jet objects are employed in the search. They are reconstructed from noise-suppressed topological calorimeter energy clusters [55] (*"small-R"* and *"large-R"* jets) or inner detector tracks (*"track"* jets) using the anti-k_t jet clustering algorithm [56] with different values of the radius parameter R.

Small-R jets (j) with the radius parameter $R = 0.4$ are used to identify vector bosons with a relatively low boost. Central jets (forward jets) within $|\eta| < 2.5$ ($2.5 \leq |\eta| < 4.5$) are required to satisfy $p_{\mathrm{T}} > 20$ GeV ($p_{\mathrm{T}} > 30$ GeV). The small-R jets satisfying $p_{\mathrm{T}} < 60$ GeV and $|\eta| < 2.4$ are required to be associated to the primary vertex using the jet-vertex-tagger discriminant [57] in order to reject the jets originating from pile-up vertices. The vertex with the highest $\sum p_{\mathrm{T}}^2$ of reconstructed tracks is selected as the primary vertex. Jet energy scale and resolution, as well as the corresponding systematic uncertainties are determined with simulation and data at $\sqrt{s} = 13$ TeV [58, 59]. Jets within $|\eta| < 2.5$ containing the b-hadrons are identified using the MV2c10 b-tagging algorithm [60–62] at an operating point with a 70% b-tagging efficiency in a simulated sample of $t\bar{t}$ events.

Large-R jets (J) [63, 64] are reconstructed with the radius parameter of $R = 1.0$ to allow for the detection of merged particle jets from a boosted vector boson decay. The trimming algorithm [65] is applied to remove the energy deposits from pile-up, the underlying event and soft radiation by reclustering the large-R jet constituents into sub-jets with radius parameter $R = 0.2$. The sub-jets with transverse momenta below 5% of the original jet transverse momentum are removed from the large-R jet. The jet mass is calculated as the resolution-weighted mean of the mass measured using only calorimeter information and the track-assisted mass measurement [66]. Large-R jets are required to satisfy $p_{\mathrm{T}} > 200$ GeV and $|\eta| < 2.0$. In the mono-W/Z search, these jets are tagged as originating from a hadronic W or Z boson decay using p_{T}-dependent requirements on the jet mass and substructure variable $D_2^{(\beta=1)}$ [67, 68]. The latter is used to select jets with two distinct concentrations of energy within the large-R jet [69, 70]. The jet mass and $D_2^{(\beta=1)}$ selection criteria are adjusted as a function of jet p_{T} to select W or Z bosons with a constant efficiency of 50% using simulated samples. In the mono-Z' search, large-R jets are tagged as originating from the hadronic decay of a Z' boson using a jet-mass requirement as well as an upper threshold $D_2^{(\beta=1)}$ <1.2, chosen to optimize the search sensitivity. The momenta of both the large-R and small-R jets are corrected for energy losses in passive material and for the non-compensating response of the calorimeter. Small-R jets are also corrected for the average additional energy due to pile-up interactions.

Track jets with the radius parameter $R = 0.2$ [71] are used to identify large-R jets containing b-hadrons [72]. The inner detector tracks originating from the primary vertex are selected by the impact parameter requirements for the track jet reconstruction. Track jets are required to satisfy $p_{\mathrm{T}} > 10$ GeV and $|\eta| < 2.5$, and are matched to the large-R jets via ghost-association [73]. Similarly as for the small-R jets, the track jets containing b-hadrons are identified using the MV2c10 algorithm at a working point with 70% efficiency.

Simulated jets are labeled according to the flavor of the hadrons with $p_{\mathrm{T}} > 5$ GeV which are found within a cone of size $\Delta R = \sqrt{\Delta\phi^2 + \Delta\eta^2} = 0.3$ around the jet axis. If a b-hadron is found, the jet is labeled as a b-jet. If no b-hadron, but a c-hadron is found, the jet is labeled as a c-jet. Otherwise the jet is labeled as light jet (l) originating from the u, d, or s-quarks or gluons. Simulated V+jets events are categorized according to this particle-level labeling into three separate categories: V + heavy flavor (V+HF) events, $V + cl$ events and V + light flavor (V+LF) events. The first category consist of $V + bb$, $V + bc$, $V + cc$ and $V + bl$ components, while the last one is given by the $V + ll$ component alone. In the very rare case that after the final selection only one jet is present in addition to the V boson, the missing jet is labeled as a light jet.

Electron candidates are reconstructed from energy clusters in the electromagnetic calorimeter that are associated to an inner detector track. The candidate electrons are identified using a likelihood-based procedure [74, 75] in combination with additional track hit requirements. All electrons, including those employed for the electron veto in the signal and in the one-muon and two-muon control regions, must satisfy the 'loose' likelihood criteria. An additional, more stringent criteria is applied in the two-electron control region, requiring that at least one of the electrons passes the 'medium' likelihood criteria. Each electron is required to have $p_{\mathrm{T}} > 7$ GeV, and $|\eta| < 2.47$, with their energy calibrated as described in [76]. To suppress the jets misidentified as electrons, electron isolation is required, defined as an upper threshold on the scalar sum of the p_{T}^{i} of the track i within a cone of size $\Delta R = 0.2$ around the electron, $(\sum p_{\mathrm{T}}^{i})^{\Delta R=0.2}$, relative to electron p_{T}. The electron p_{T} is subtracted from the sum. The p_{T}- and η-dependent thresholds corresponding to the isolation efficiency of 99% are applied. In addition, to suppress the electrons not originating from the primary vertex, upper thresholds are set on the longitudinal impact parameter, $|z_0 \sin\theta| < 0.5$ mm, and the transverse impact parameter significance, $|d_0|/\sigma(d_0)$ <5.

Muon candidates are primarily reconstructed from a combined fit of inner detector hits and muon spectrometer segments [77]. In the central detector region ($|\eta| < 0.1$) lacking the muon spectrometer coverage, the muons are also identified by matching a fully reconstructed inner detector track to the calorimeter energy deposits consistent with a minimum ionizing particle. Two identification working points with increasing purity are used. All muons, including those employed for the muon veto in the signal and in the two-electron control regions, must satisfy the 'loose' likelihood criteria. In addition, the muon in the one-muon control region and at least one of the two muons in the two-muon control region must pass the 'medium' likelihood criteria. Each muon is required to have $p_{\mathrm{T}} > 7$ GeV and $|\eta| < 2.7$ and satisfy the impact parameter criteria $|z_0 \sin\theta| < 0.5$ mm and $|d_0|/\sigma(d_0)$ <3. Primarily, all muons are required to be isolated by requiring an upper threshold on the scalar sum $(\sum p_{\mathrm{T}}^{i})^{\Delta R=0.3}$ relative to the muon p_{T} that corresponds to a 99% isolation efficiency, similarly as for the electrons. Only in the one-muon control region, tighter isolation criteria with $(\sum p_{\mathrm{T}}^{i})^{\Delta R=0.3}/p_{\mathrm{T}}$ <0.06 are applied. In both cases, the muon p_{T} is subtracted from the scalar sum.

The vector of the missing transverse momentum $\boldsymbol{E}_{\mathbf{T}}^{\mathbf{miss}}$ is calculated as the negative vector sum of the transverse momenta of calibrated small-R jets and leptons, together with the tracks which are associated to the primary interaction vertex but not associated to any of these physics objects [78]. A closely related quantity, $\boldsymbol{E}_{\mathbf{T}}^{\mathbf{miss(no\ lepton)}}$, is calculated in the same way but excluding the reconstructed muons or electrons. The missing transverse momentum is given by the magnitude of these vectors, $E_{\mathrm{T}}^{\mathrm{miss}} = |\boldsymbol{E}_{\mathbf{T}}^{\mathbf{miss}}|$ and $E_{\mathrm{T}}^{\mathrm{miss(no\ lepton)}} = |\boldsymbol{E}_{\mathbf{T}}^{\mathbf{miss(no\ lepton)}}|$. In addition, the track-based missing transverse momentum vector, $\boldsymbol{p}_{\mathbf{T}}^{\mathbf{miss}}$, and similarly $\boldsymbol{p}_{\mathbf{T}}^{\mathbf{miss(no\ lepton)}}$, is calculated as the negative vector sum of the transverse momenta of tracks with $p_{\mathrm{T}} > 0.5$ GeV and $|\eta| < 2.5$ originating from the primary vertex.

6 Event selection and categorization

Events studied in this analysis are accepted by the combination of $E_{\mathrm{T}}^{\mathrm{miss}}$ triggers with thresholds between 70 GeV and 110 GeV, depending on the data taking periods. The trigger efficiency is measured in data using events with large $E_{\mathrm{T}}^{\mathrm{miss}}$ accepted by the muon triggers. The triggers are found to be fully efficient for $E_{\mathrm{T}}^{\mathrm{miss}} > 200$ GeV and the inefficiency at lower $E_{\mathrm{T}}^{\mathrm{miss}}$ values and the corresponding uncertainty are taken into account. At least one collision vertex with at least two associated tracks is required in each event and for the signal region selection a veto is imposed on all events with loose electrons or muons in

the final state. Depending on the Lorentz boost of the vector boson, two distinctive event topologies are considered: a *merged topology* where the decay products of the vector boson are reconstructed as a single large-R jet and a *resolved topology* where they are reconstructed as individual small-R jets. Each event is first passed through the merged-topology selection and, in case of failure, passed further through the resolved-topology selection. Thus, there is no overlap of events between the two final-state topologies. For the mono-Z' search, the categorization into merged and resolved event topologies is only performed for the mediator mass hypothesis of $m_{Z'}$ below 100 GeV. For heavier mediator masses, the angular separation of jets from the Z' boson decay is expected to be larger than the size of a large-R jet. Thus, only the resolved-topology selection criteria are applied in this case.

The mono-W/Z and mono-Z' event selection criteria applied for each of the two topologies are summarized in Table 2. The criteria have been optimized to obtain the maximum expected signal significance. In the merged (resolved) event topology, at least one large-R jet (at least two small-R jets) and $E_{\mathrm{T}}^{\mathrm{miss}}$ values above 250 GeV (above 150 GeV) are required in the final state. In order to suppress the $t\bar{t}$ and V+jets background with heavy-flavor jets, all events with merged topology containing b-tagged track jets not associated to the large-R jet via ghost-association are rejected. In the resolved topology, all events with more than two b-tagged small-R jets are rejected. The highest-p_{T} large-R jet in an event is considered as the candidate for a hadronically decaying vector boson in the merged topology. Similarly, in the resolved topology the two leading b-tagged small-R jets are selected as the candidate for a hadronically decaying W or Z boson and, in case of less than two b-jets in the final state, the highest-p_{T} remaining jets are used to form the hadronic W or Z boson decay candidate. Additional criteria are applied in both merged and resolved topologies to suppress the contribution of multijet events. Since the vector bosons in signal events are recoiling against the dark matter particles, a lower threshold is applied on the azimuthal distance between the $\boldsymbol{E}_{\mathbf{T}}^{\mathbf{miss}}$ vector and the highest-p_{T} large-R jet (system of the two highest-p_{T} jets) in the merged (resolved) topology, $\Delta\phi(\boldsymbol{E}_{\mathbf{T}}^{\mathbf{miss}}, J \text{ or } jj) > 120^{\mathrm{o}}$. Also, the angles between $\boldsymbol{E}_{\mathbf{T}}^{\mathbf{miss}}$ and the three highest-p_{T} small-R jets should be sufficiently large, $\min\left[\Delta\phi(\boldsymbol{E}_{\mathbf{T}}^{\mathbf{miss}}, \mathrm{j})\right] > 20^{\mathrm{o}}$ in order to suppress events with a significant $E_{\mathrm{T}}^{\mathrm{miss}}$ contribution from mis-measured jets. Events with a large $E_{\mathrm{T}}^{\mathrm{miss}}$ value originating from the calorimeter mis-measurements can be additionally suppressed by the requirement of a non-vanishing track-based missing transverse momentum, $p_{\mathrm{T}}^{\mathrm{miss}} > 30$ GeV, and the requirement on the azimuthal distance between the calorimeter-based and track-based missing transverse momenta, $\Delta\phi(\boldsymbol{E}_{\mathbf{T}}^{\mathbf{miss}}, \boldsymbol{p}_{\mathbf{T}}^{\mathbf{miss}}) < 90^{\mathrm{o}}$. The $p_{\mathrm{T}}^{\mathrm{miss}}$ requirements also reduce non-collision background from beam halos or beam gas interactions that produce signal in time with the colliding proton bunches. Such events are characterized mainly by energy deposits in calorimeters in the absence of track activity. In the categories with two b-tagged jets the non-collision background is negligible and the expected discovery significance is higher without the $p_{\mathrm{T}}^{\mathrm{miss}}$ requirement. Further criteria are imposed on events with the resolved topology. The highest-p_{T} (leading) jet is required to have $p_{\mathrm{T}}^{j_1} > 45$ GeV. To improve the trigger efficiency modeling with MC events, the scalar sum of the transverse momenta of all jets is required to be $\sum p_{\mathrm{T}}^{j_i} > 120$ (150) GeV in events with two (at least three) jets.

After these general requirements, the events are classified according to the number of b-tagged jets into events with exactly zero ($0b$), one ($1b$) and two ($2b$) b-tagged jets to improve the signal-to-background ratio and the sensitivity to $Z \to bb$ decays. Small-R jets (track jets) are used for the b-tagging in the resolved (merged) category. Further selection criteria defining the final signal regions are introduced separately for the mono-W/Z and mono-Z' searches.

For the mono-W/Z search, the events in $0b$ and $1b$ categories with merged topology are further classified into high-purity (HP) and low-purity (LP) regions; the former category consists of events satisfying the

p_{T}-dependent requirements on the jet substructure variable $D_2^{(\beta=1)}$, allowing an improved discrimination for jets containing $V \to q\bar{q}$ decays, while the latter one selects all the remaining signal events. In the signal region with resolved topology, the angular distance ΔR_{jj} between the two leading jets is required to be smaller than 1.4 (1.25) in the $0b$ and $1b$ ($2b$) categories. Finally, a mass window requirement is imposed on the vector boson candidate in each of the eight resulting signal categories. In the $0b$ and $1b$ merged-topology categories, a mass requirement depending on the large-R jet p_{T} is applied. The large-R jet mass and $D_2^{(\beta=1)}$ requirements have been optimized within a dedicated study of the W/Z tagger performance [63, 64]. In the $2b$ merged-topology category, in which the signal is expected to come predominantly from $Z \to bb$ decays, a mass window requirement of 75 GeV $< m_J <$ 100 GeV is applied. The large-R jet substructure variable $D_2^{(\beta=1)}$ is not considered in this channel in order to obtain a higher signal efficiency and higher expected discovery significance. In the resolved $0b$ and $1b$ ($2b$) categories, the mass of the dijet system composed of the two leading jets is required to be 65 GeV $< m_{jj} <$ 105 GeV (65 GeV $< m_{jj} <$ 100 GeV). For the mono-Z' search, a similar classification by the b-tagging multiplicity, and by the substructure variable $D_2^{(\beta=1)}$ into high- and low-purity regions in the merged-topology category, is performed, using slightly different requirements on the substructure of the large-R jet. A p_{T}-independent threshold on the substructure variable $D_2^{(\beta=1)}$ is set at the value of 1.2 in signal regions with merged topology, as it is found to provide the maximum expected signal significance. Additional criteria also differ from the criteria applied in the mono-W/Z search. No criteria are applied on the ΔR_{jj} variable in events with the resolved topology, since the high-mass Z' bosons in dark-fermion or dark-Higgs models are less boosted than W or Z bosons in the simplified vector-mediator model, leading to a larger angular separation of jets from the Z' boson decays. The requirements on the mass of the Z' candidate are optimized for each event category as summarized in Table 2.

For both the mono-W/Z and the mono-Z' search, the $E_{\mathrm{T}}^{\mathrm{miss}}$ distribution in each event category is used as the final discriminant for the statistical interpretation of the data, since for the models with very large $E_{\mathrm{T}}^{\mathrm{miss}}$ values a better sensitivity can be achieved compared to the V candidate mass discriminant. The $E_{\mathrm{T}}^{\mathrm{miss}}$ distributions after the full selection, as well as the m_J and m_{jj} distributions before the mass window requirement are shown for various signal models in Figures 2 and 3.

Figure 4 shows the product $(\mathcal{A} \times \varepsilon)_{\mathrm{total}}$ of the signal acceptance $\mathcal{A}$ and selection efficiency ε for the simplified vector-mediator model and for the dark-fermion and dark-Higgs mono-Z' signal models after the full event selection. This product is defined as the number of signal events satisfying the full set of selection criteria, divided by the total number of generated signal events. For all signal models, the main efficiency loss is caused by the minimum $E_{\mathrm{T}}^{\mathrm{miss}}$ requirement.

In the simplified vector-mediator model, the $(\mathcal{A} \times \varepsilon)_{\mathrm{total}}$, obtained by summing up signal contributions from all event categories, increases from 1% for low to 15% for high mediator mass due to the increase of the missing transverse momentum in the final state.

Similarly, for the mono-Z' signal models, the $(\mathcal{A} \times \varepsilon)_{\mathrm{total}}$ increases with increasing mediator mass from 2% to 15% (from a few % to up to 40%) in scenarios with a light (heavy) dark sector. The $(\mathcal{A} \times \varepsilon)_{\mathrm{total}}$ for invisible Higgs boson decays is 0.5% when summing over all introduced signal regions. About 58% of that signal originates from the ggH, 35% from the VH and 7% from the VBF production processes, with $(\mathcal{A} \times \varepsilon)_{\mathrm{total}}$ of 0.3%, 5.7% and 0.5%, respectively.

The number of signal events in a given signal-region category, relative to the total number of signal events selected in all signal categories, depends on the signal model and mediator mass. The largest fraction is expected in the $0b$ category with resolved topology, where it ranges from 40% to 80%. This is followed by the $0b$-HP and $0b$-LP merged-topology categories with 10% to 20% of signal events in each of the two.

Table 2: Event selection criteria in the mono-W/Z and mono-Z' signal regions with merged and resolved event topologies. The symbols "j" and "J" denote the reconstructed small-R and large-R jets, respectively. The abbreviations HP and LP denote respectively the high- and low-purity signal regions with merged topology, as defined by the cut on the large-R jet substructure variable $D_2^{(\beta=1)}$.

	Merged topology	**Resolved topology**
General requirements		
$E_{\mathrm{T}}^{\mathrm{miss}}$	> 250 GeV	> 150 GeV
Jets, leptons	$\geq 1J, 0\ell$	$\geq 2j, 0\ell$
b-jets	no b-tagged track jets outside of J	≤ 2 b-tagged small-R jets
Multijet suppression	$\Delta\phi(\boldsymbol{E}_{\mathbf{T}}^{\mathbf{miss}}, J \text{ or } jj) > 120^{\mathrm{o}}$ $\min_{i\in\{1,2,3\}} \left[\Delta\phi(\boldsymbol{E}_{\mathbf{T}}^{\mathbf{miss}}, j_i)\right] > 20^{\mathrm{o}}$ $p_{\mathrm{T}}^{\mathrm{miss}} > 30$ GeV or ≥ 2 b-jets $\Delta\phi(\boldsymbol{E}_{\mathbf{T}}^{\mathbf{miss}}, \boldsymbol{p}_{\mathbf{T}}^{\mathbf{miss}}) < 90^{\mathrm{o}}$	
Signal properties		$p_{\mathrm{T}}^{j_1} > 45$ GeV $\sum p_{\mathrm{T}}^{j_i} > 120$ (150) GeV for 2 (≥ 3) jets

Mono-W/Z signal regions

	0b HP	**0b LP**	**1b HP**	**1b LP**	**2b**	**0b**	**1b**	**2b**
ΔR_{jj}	-	-	-	-	-	< 1.4	< 1.4	< 1.25
$D_2^{(\beta=1)}$ p_{T}^J-dep.	pass	fail	pass	fail	-	-	-	-
Mass requirement (GeV)	m_J W/Z tagger requirement				m_J [75, 100]	m_{jj} [65, 105]		m_{jj} [65, 100]

Mono-Z' signal regions

	0b HP	**0b LP**	**1b HP**	**1b LP**	**2b**	**0b**	**1b**	**2b**
$D_2^{(\beta=1)}$ <1.2	pass	fail	pass	fail	-	-	-	-
Mass requirement (GeV)	For $m_{Z'} < 100$ GeV:					For $m_{Z'} < 200$ GeV:		
	$[0.85m_{Z'}, m_{Z'} + 10]$		$[0.75m_{Z'}, m_{Z'} + 10]$			$[0.85m_{Z'}, m_{Z'} + 10]$	$[0.75m_{Z'}, m_{Z'} + 10]$	
	For $m_{Z'} \geq 100$ GeV:					For $m_{Z'} \geq 200$ GeV:		
	no merged-topology selection applied					$[0.85m_{Z'}, m_{Z'} + 20]$	$[0.80m_{Z'}, m_{Z'} + 20]$	

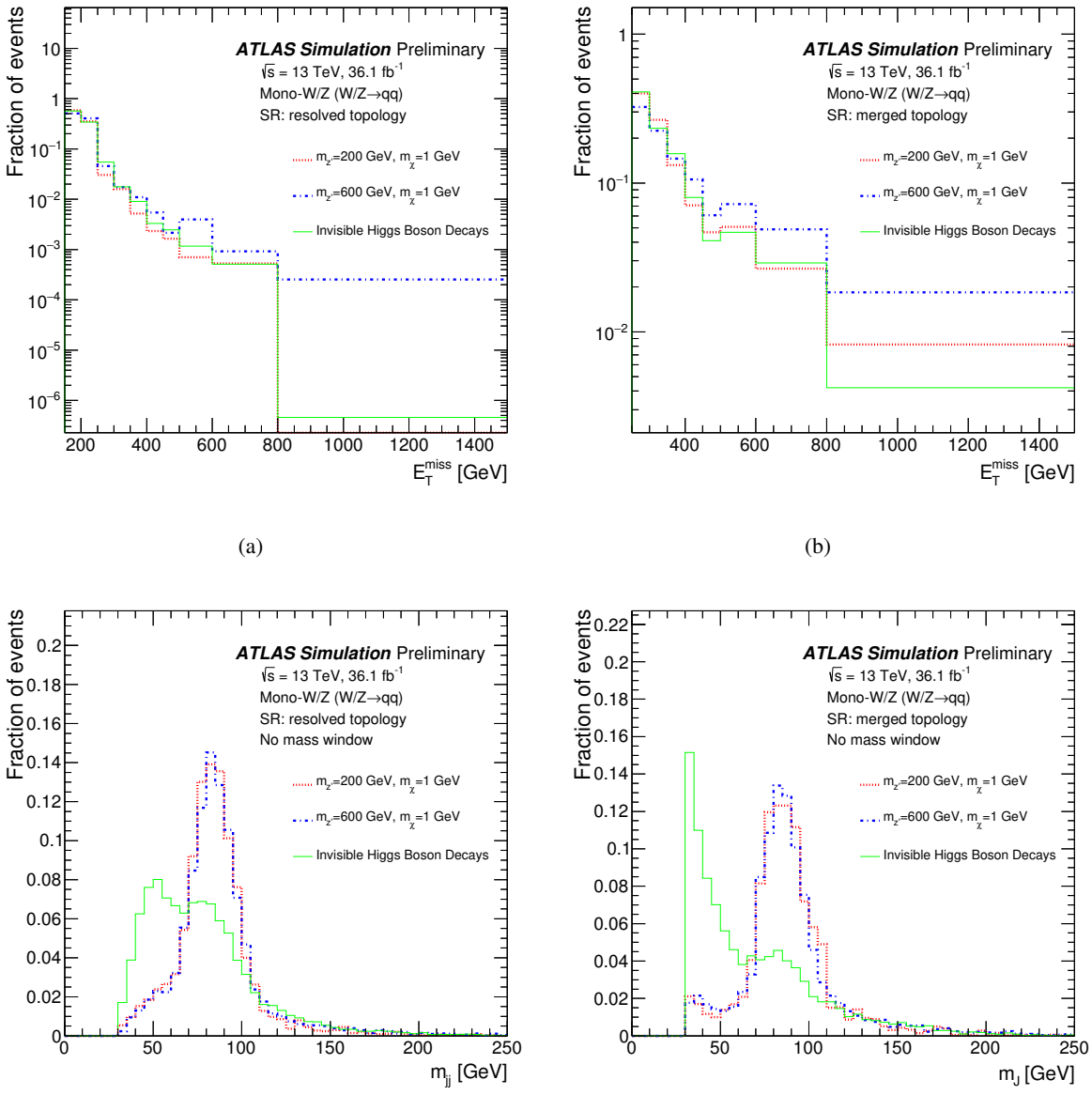

Figure 2: Expected $E_{\mathrm{T}}^{\mathrm{miss}}$ distributions, normalized to unit area, for the simplified vector-mediator model and invisible Higgs boson decays after the full selection in the resolved (a) and merged (b) event topologies and the expected invariant mass distribution m_{jj} in the resolved (c) and m_J in the merged (d) event topology before the mass window requirement. The signal contributions from each resolved (merged) category are summed together.

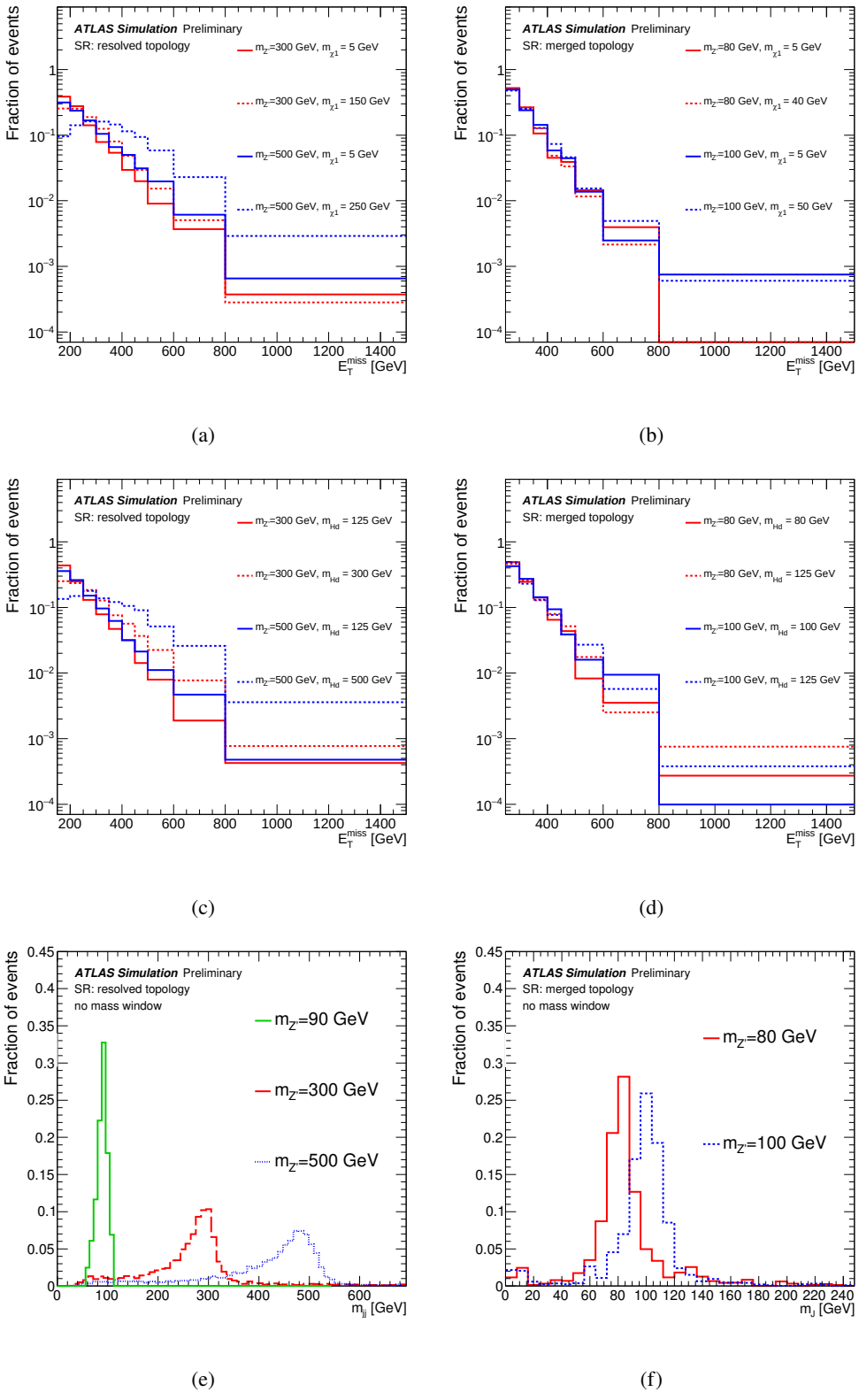

Figure 3: Expected $E_{\mathrm{T}}^{\mathrm{miss}}$ distributions, normalized to unit area, after the full selection for the dark-fermion mono-Z' model in the resolved (a) and merged (b) event topologies, dark-Higgs mono-Z' model in the resolved (c) and merged (d) event topologies, as well as the expected invariant mass distribution m_{jj} in the resolved (e) and m_J in the merged (f) event topologies for the dark-fermion mono-Z' model in the light dark-sector scenario before the mass window requirement. Similar mass distributions are also seen for other mono-Z' models.

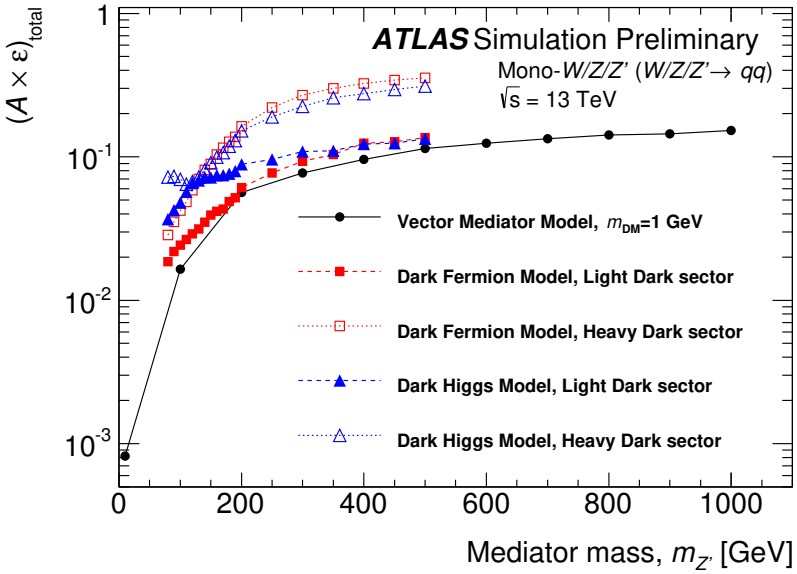

Figure 4: The product of acceptance and efficiency $(\mathcal{A} \times \varepsilon)_{\text{total}}$, defined as the number of signal events satisfying the full set of selection criteria, divided by the total number of generated signal events, after the full event selection for the combined mono-W and mono-Z signal of the simplified vector-mediator model and for the mono-Z' dark-fermion and dark-Higgs signal models, shown in dependence on the mediator mass $m_{Z'}$. For a given model, the signal contributions from each category are summed together. The lines are drawn just to guide the eye.

In case of the mono-Z' signal models, also the $1b$ and $2b$ categories with resolved topology contain about 7% to 10% of the total signal contribution. The signal contributions in every other category are below 5%.

7 Background estimation

The dominant background contribution in the signal region originates from the $t\bar{t}$ and V+jets production. In the latter case, mostly decays of Z bosons into neutrinos ($Z \to \nu\nu$) and $W \to \tau\nu$ contribute, as well as $W \to (e\nu, \mu\nu)$ with non-identified electrons and muons. The normalization of the $t\bar{t}$ and V+jets background processes and the corresponding shapes of the final $E_{\text{T}}^{\text{miss}}$ discriminant are constrained using two dedicated background-enriched data control regions with leptons in the final state. The multijet background contribution is estimated by employing additional multijet-enriched control regions. Events in each control region are selected using criteria similar, while at the same time disjoint, to those in the signal region. Events are also categorized into merged and resolved topologies, each divided into three categories with different b-tagged jet multiplicities. No requirement is imposed on the large-R jet substructure and therefore there is no further classification of the merged-topology events into the low- and high-purity control regions, as is the case for the signal regions. The remaining small contributions from the diboson and single-top-quark production are determined from simulation.

The two control regions with one and two leptons in the final state are defined to constrain the W+jets and Z+jets backgrounds, respectively, together with the $t\bar{t}$ contribution in the one lepton control region. The latter process is dominant in $2b$ control region categories. In order to increase the event yield, no

requirement is imposed on the large-R jet substructure or ΔR_{jj} in the merged and resolved topologies, respectively. The *one-lepton control region* is defined by requiring no 'loose' electrons and exactly one muon with 'medium' identification with $p_{\mathrm{T}} > 25$ GeV and tight isolation criteria in the final state. Events are collected by $E_{\mathrm{T}}^{\mathrm{miss}}$ triggers, as these triggers enhance most efficiently contributions from events with a signal-like topology. The *two-lepton control region* consists of events passing the single-lepton trigger. One of the two reconstructed leptons has to be matched to the corresponding lepton trigger. A pair of 'loose' muons or electrons with the invariant dilepton mass $66 < m_{\ell\ell} < 116$ GeV is required in the final state. At least one of the two leptons is required to have $p_{\mathrm{T}} > 25$ GeV and to satisfy the stricter 'medium' identification criteria. To emulate the missing transverse energy from non-reconstructed leptons (neutrinos) in W (Z) boson decays in the event selection, the $E_{\mathrm{T}}^{\mathrm{miss(no\ lepton)}}$ and $p_{\mathrm{T}}^{\mathrm{miss(no\ lepton)}}$ variables are used instead of $E_{\mathrm{T}}^{\mathrm{miss}}$ and $p_{\mathrm{T}}^{\mathrm{miss}}$, respectively. The $E_{\mathrm{T}}^{\mathrm{miss(no\ lepton)}}$ distribution is employed for the statistical interpretation as the final discriminant in these control regions. The control region data are also used to confirm the good modeling of other discriminant variables such as the invariant mass of the vector boson candidate or the large-R jet substructure variable $D_2^{(\beta=1)}$ in events with signal-like topology.

The multijet background contribution is estimated separately for each signal region category from a *multijet control region* selected by inverting the most effective requirement to discriminate multijet events in the signal region, i.e. $\min\Delta\phi(\boldsymbol{E}_{\mathrm{T}}^{\mathrm{miss}}, \mathrm{j}) \equiv \min\Delta\phi < 20^{\mathrm{o}}$. The $E_{\mathrm{T}}^{\mathrm{miss}}$ distribution observed in that region is used as an expected multijet background shape after a simulation-based subtraction of a small contribution of non-multijet backgrounds. To account for the inversion of the $\min\Delta\phi$ requirement, the distribution is scaled by the corresponding normalization scale factor. This normalization scale factor is determined in an equivalent control region, but with both the $\min\Delta\phi$ and $\Delta\phi(\boldsymbol{E}_{\mathrm{T}}^{\mathrm{miss}}, \boldsymbol{p}_{\mathrm{T}}^{\mathrm{miss}})$ requiremens removed and the mass window criteria inverted to select only events in the mass sidebands. In that new control region, the $E_{\mathrm{T}}^{\mathrm{miss}}$ distribution from events with $\min\Delta\phi < 20^{\mathrm{o}}$ is fitted to the data with $\min\Delta\phi > 20^{\mathrm{o}}$, together with other background contributions, and the resulting normalization factor is applied on the $E_{\mathrm{T}}^{\mathrm{miss}}$ distribution from the multijet control region. For the mono-W/Z search, the high-mass sideband is used, ranging from the upper mass window threshold up to 250 GeV. Since ΔR_{jj} and $\Delta\phi_{jj}$ criteria are not applied in case of the mono-Z' search, the event topology in the high-mass sideband is in general not close enough to the topology of the signal region. Therefore, the low-mass sideband is used for the estimate of the multijet contribution in the mono-Z' search. The sideband mass range depends on the mass of the Z' boson: the upper sideband bound is set at the lower bound of the signal region mass window and the size of the sideband is the same as the size of the mass window in the signal region. With the described method, the multijet contribution is estimated to contribute up to a few percent of the total background yield depending on the signal category. The contribution of the multijet background in the 1-lepton and 2-lepton control regions is negligible.

For the mono-W/Z searches, all background contributions are additionally constrained by the *mass sideband regions* in the 0-lepton final state. These regions are defined by the same selection criteria introduced in Section 6, except for the requirements on the large-R jet and di-jet mass values, which are required to be above the signal mass window and below 250 GeV. Events in this region are topologically and kinematically very similar to those in the full signal region, with a similar background composition. The corresponding sideband regions are also introduced for the one-lepton and the two-lepton control regions. While there is no signal contamination expected in the one-lepton and two-lepton control regions, the signal contribution in the 0-lepton mass sideband region is not negligible. Compared to the total signal contribution in the signal region described in the previous section, there are about 20% of additional signal events expected in the sidebands in case of the simplified vector-mediator model. For the invisible Higgs boson decays, the original signal contribution is increased by about 35% after including the sideband

region, dominated by the ggH production process. There are no sideband regions employed for the mono-Z' searches. Since the hypothesized mass of the Z' boson is a free parameter, the 0-lepton sideband regions cannot be considered free of signal contamination.

The final estimate of background contributions is obtained from a simultaneous fit of the expected final discriminants to data in all signal, sideband and control regions (see Section 9). The signal contributions in the mass sideband regions are taken into account in the fit.

8 Systematic uncertainties

Several experimental and theoretical systematic uncertainties affect the results of the presented analysis. Their impact is evaluated in each bin of a $E_{\mathrm{T}}^{\mathrm{miss}}$ distribution. In this section, the impact of different sources of uncertainties on the expected signal and background yields is summarized, while the overall impact on the final results is discussed in the next section.

The impact of theoretical uncertainties on the signal yield due to variations of the QCD renormalization and factorization scale, uncertainties on the parton distribution functions, as well as the underlying event and parton shower description are estimated to be about 10-15% for the simplified vector-mediator model. For the invisible decays of the Higgs boson produced via VH and ggH processes, the theory uncertainties affect the signal yields by 5% and 10%, respectively for the resolved event topology and about two times larger for the merged topology. No systematic uncertainty on the VBF signal is considered, since it has a negligible impact on the final results. No theoretical uncertainty is considered for the mono-Z' signals, since it is negligible compared to the experimental uncertainties.

For the background processes, a number of theoretical modeling systematic uncertainties are considered, affecting mostly the expected shape of the $E_{\mathrm{T}}^{\mathrm{miss}}$ distribution. These uncertainties are estimated following the studies of Ref. [34] and are briefly summarized here. The uncertainties in the V+jets background contribution come mainly from the limited knowledge of the jet flavor composition in terms of the V+HF categorization introduced in Section 5, as well as the modeling of the vector boson transverse momentum (p_{T}^{V}) and dijet mass (m_{jj}) distributions. The former are evaluated by means of scale variations in the generated Sherpa samples. In addition to this, the difference between the Sherpa nominal sample and an alternative MadGraph5_aMC@NLO v2.2.2 sample produced with a different matrix-element generator is added in quadrature to yield the total uncertainty. The uncertainty in the modeling of the p_{T}^{V} and m_{jj} distributions is obtained from the comparison of simulated events with dedicated control region data, as well as comparisons with alternative generator predictions. For the $t\bar{t}$ production, uncertainties in the shapes of top quark transverse momentum and the m_{jj} and p_{T}^{V} distributions of the V boson candidate are considered by comparing the nominal simulated sample to alternative samples with different parton shower, matrix element generation and tuning parameters. A similar procedure is applied also for the diboson and single top quark backgrounds. While the overall V+jets and $t\bar{t}$ normalization is determined from the fit to data, the comparison of different generators is also employed to assign a normalization uncertainty for the single top quark and diboson production since their contributions are estimated from simulation.

The uncertainty of 100% is assigned on the multijet normalization in both the mono-W/Z and mono-Z' searches due to the statistical uncertainty of the control data, the impact of non-multijet backgrounds and the extrapolation from multijet control regions to signal regions. The shape of the multijet background

distributions is subject to an uncertainty on the order of 10%, depending on the amount of non-multijet background in each signal region.

In case of both mono-W/Z and mono-Z' searches, the largest source of experimental systematic uncertainties in the merged topology is the modeling of the large-R jet properties. The large-R jet mass scale and resolution uncertainty has an up to 5% impact on the expected background yields and up to 5%, 10% and 15% impact on the signal yields from invisible Higgs boson decays, simplified vector-mediator model and mono-Z' models, respectively. The uncertainty in the large-R jet energy resolution affects the simplified vector-mediator signal by 3% and background by 1%. The impact on the mono-Z' signal and the signal from invisible Higgs boson decays is at the sub-percent level. The uncertainty in the scale of the $D_2^{(\beta=1)}$ substructure parameter affects the migration between the high-purity and low-purity regions, with a 5-10% (2-5%) impact on the background (mono-W/Z and mono-Z' signal) yields. The combined impact of all other large-R jet uncertainties is below a few percent. The combined impact of large-R jet uncertainties on events within the resolved-topology categories is negligible for the mono-W/Z search and below 2% for the mono-Z' searches. The small-R jet uncertainties are dominated by the energy scale and resolution uncertainties. The small-R jet energy scale uncertainty has an up to 10% (up to 6%) impact on the background (signal) yields. The uncertainty in the small-R jet energy resolution has a 2-5% impact on the signal yields. The corresponding impact of this uncertainty on the background yield is at a sub-percent level in the mass window around the W and Z boson mass, growing to around 1.5% for the mono-Z' search in the mass window around $m_{Z'} = 500$ GeV. The b-tagging calibration uncertainty affects the migration of signal and background events between categories with different b-tag multiplicities by up to 10%. The uncertainty in the missing transverse momentum component which is not associated to any of the selected objects with high transverse momentum affects the background (signal) yields by about 1-3% (2-10%). The uncertainties in the trigger efficiency, lepton reconstruction and identification efficiency, as well as the lepton energy scale and resolution affect the signal and background contributions only at a sub-percent level.

The uncertainty in the combined 2015+2016 integrated luminosity is 2.1%. It is derived, following a methodology similar to that detailed in Ref. [79], from a calibration of the luminosity scale using x-y beam-separation scans performed in August 2015 and May 2016.

9 Results

A profile likelihood fit [80] is used for the interpretation of the data in search for dark matter production. A fit to the data is performed using the likelihood function defined as the product of conditional probabilities P over binned distributions of discriminating observables in each event category j,

$$\mathcal{L}(\mu, \boldsymbol{\theta}) = \prod_{j}^{N_{\text{categories}}} \prod_{i}^{N_{\text{bins}}} P\left(N_{ij} \,|\mu S_{ij}(\boldsymbol{\theta}) + B_{ij}(\boldsymbol{\theta})\right) \prod_{k}^{N_{\text{nuisance}}} \mathcal{G}(\theta_k) \,.$$

The likelihood function depends on the signal strength μ, defined as the signal yield relative to the prediction from simulation, and on the vector of nuisance parameters $\boldsymbol{\theta}$ accounting for the background normalization and systematic uncertainties introduced in Section 8. The Poisson distributions P correspond to the observation of N_{ij} events in each bin i of the discriminating observable given the expectations for the background, $B_{ij}(\boldsymbol{\theta})$, and for the signal, $S_{ij}(\boldsymbol{\theta})$. A constraint on a nuisance parameter θ_k is represented by

the Gaussian function $\mathcal{G}(\theta_k)$. The correlations between nuisance parameters across signal and background processes and categories are taken into account.

For the mono-W/Z search, the event categories include all eight 0-lepton signal regions (see Section 6), six one-lepton and six two-lepton control regions, as well as the corresponding sideband regions for each of these twenty categories (see Section 7). In comparison, no sideband regions are employed for the mono-Z' search and only categories with the resolved topology are considered for $m_{Z'} > 100$ GeV. In the 0-lepton signal and sideband regions, the $E_{\mathrm{T}}^{\mathrm{miss}}$ distribution is used as the discriminating variable since the signal process results in relatively large $E_{\mathrm{T}}^{\mathrm{miss}}$ values compared to the backgrounds. In order to constrain the backgrounds and the $E_{\mathrm{T}}^{\mathrm{miss}}$ shapes, in the signal region, the $E_{\mathrm{T}}^{\mathrm{miss(no\ lepton)}}$ variables are used in the fit in the one- and two-lepton control regions. The normalizations of the W+HF, W+LF, Z+HF, Z+LF and $t\bar{t}$ background components are treated as unconstrained parameters in the fit, independent from each other and correlated across all event categories. The uncertainties on the flavor composition of the V+HF processes are taken into account following the studies outlined in Section 8. The normalization of other background components is constrained according to their theory uncertainty. A possible difference between the normalization factors in events with resolved and merged topologies for the W+jets, Z+jets and $t\bar{t}$ processes due to systematic modeling effects is taken into account by means of two additional constrained nuisance parameters. The multijet contribution is only considered in the signal regions and the corresponding mass sidebands, with decorrelated normalization factors for each category.

The normalization of the W+HF, W+LF and Z+LF background components obtained from the fit to the data under the background-only hypothesis is in a good agreement with the SM expectation, while the Z+HF ($t\bar{t}$) normalization is 30% higher (20% lower) than the expected SM value. In addition to the normalization factors, the final background event yields in each event category are also affected by the systematic uncertainties discussed in Section 8. For all backgrounds other than Z+HF and $t\bar{t}$, the number of background events obtained from the fit agrees well with the prediction from simulation in each event category individually. The number of observed events passing the final mono-W/Z signal selection is shown for each event category in Table 3 together with the expected background contributions obtained from the fit under the background-only hypothesis. The expectations for several signal points within the simplified vector-mediator model and for the invisible Higgs boson decays are shown in addition for comparison. Figure 5 and 6 show the corresponding distributions of the missing transverse energy in the merged and resolved mono-W/Z signal regions, respectively.

Similarly, the number of observed and expected events passing the final mono-Z' selection is shown in Tables 4 and 5 for mediator masses $m_{Z'}$ of 90 GeV and 300 GeV, respectively. The expected and observed numbers of background events for the $m_{Z'}$ hypothesis of 90 GeV are similar to those from the mono-W/Z search in all categories, except for the 2b-tag category with resolved topology. There are about three times more events in that category for the mono-Z' search, since no requirement on ΔR_{jj} is applied, as opposed to the strict requirement of $\Delta R_{jj} < 1.25$ employed in the mono-W/Z search. The distributions of the missing transverse energy in each mono-Z' signal region for these mediator masses are shown in Figures 7 and 8.

The impact of the different sources of systematic uncertainties on the sensitivity of the mono-W/Z and mono-Z' searches is estimated by means of the fits of the signal-plus-background model to hypothetical data comprized of these signals (with signal strength $\mu = 1$) and of expected background contributions. The resulting expected uncertainties on the signal strength μ serve as a measure of the analysis sensitivity and are summarized in Table 6. The tests of the background-only versus the signal-plus-background hypothesis using a profile likelihood test statistic show no significant deviation from the SM expectation

Table 3: The expected and observed numbers of events for an integrated luminosity of 36.1 fb^{-1} and $\sqrt{s}$ = 13 TeV, shown separately in each mono-W/Z signal region category. The background yields and uncertainties are shown after the profile likelihood fit to the data. The quoted background uncertainties include both the statistical and systematic contributions, while the uncertainty on the signal is of statistical nature only. The uncertainties on the total background can be smaller than those on individual components due to anti-correlations of nuisance parameters.

	Merged topology				
Process	0b-HP	0b-LP	1b-HP	1b-LP	2b
Vector-mediator model,					
m_χ =1 GeV, $m_{Z'}$ =200 GeV	814 ± 48	759 ± 45	96 ± 18	99 ± 16	49.5 ± 4.3
m_χ =1 GeV, $m_{Z'}$ =600 GeV	280.9 ± 9.0	268.5 ± 8.8	34.7 ± 3.6	33.8 ± 3.1	15.38 ± 0.84
Invisible Higgs boson decays (m_H = 125 GeV, $\mathcal{B}_{H\to\text{inv.}}$ = 100%)					
VH	408.4 ± 2.1	299.3 ± 2.0	52.06 ± 0.85	44.06 ± 0.82	27.35 ± 0.52
ggH	184 ± 19	837 ± 35	11.7 ± 3.8	111 ± 30	12.3 ± 4.2
VBF	29.1 ± 2.5	96.0 ± 4.6	2.43 ± 0.36	5.83 ± 0.43	0.50 ± 0.07
W+jets	3170 ± 140	10120 ± 380	218 ± 28	890 ± 110	91 ± 12
Z+jets	4750 ± 200	15590 ± 590	475 ± 52	1640 ± 180	186 ± 12
$t\bar{t}$	775 ± 48	937 ± 60	629 ± 27	702 ± 34	50 ± 11
Single top-quark	159 ± 12	197 ± 13	89.7 ± 6.7	125.5 ± 8.7	16.1 ± 1.7
Diboson	770 ± 110	960 ± 140	88 ± 14	115 ± 18	54 ± 10
Multijet	12 ± 35	49 ± 140	3.7 ± 3.3	15 ± 13	9.3 ± 9.4
Total background	9642 ± 87	27850 ± 150	1502 ± 31	3490 ± 52	407 ± 15
Data	9627	27856	1502	3525	414

	Resolved topology		
Process	0b	1b	2b
Vector-mediator model,			
m_χ =1 GeV, $m_{Z'}$ =200 GeV	5050 ± 130	342 ± 29	136.7 ± 6.0
m_χ =1 GeV, $m_{Z'}$ =600 GeV	840 ± 16	59.9 ± 4.6	27.86 ± 0.94
Invisible Higgs boson decays (m_H = 125 GeV, $\mathcal{B}_{H\to\text{inv.}}$ = 100%)			
VH	2129.6 ± 6.4	171.7 ± 2.2	104.7 ± 1.2
ggH	4111 ± 78	178 ± 16	37 ± 11
VBF	514 ± 12	19.8 ± 2.3	2.33 ± 0.72
W+jets	117500 ± 4600	5000 ± 680	598 ± 98
Z+jets	135400 ± 5600	7710 ± 780	1219 ± 67
$t\bar{t}$	13800 ± 780	12070 ± 420	2046 ± 70
Single top-quark	2360 ± 140	1148 ± 71	222 ± 14
Diboson	6880 ± 950	514 ± 71	228 ± 34
Multijet	11900 ± 2300	1130 ± 370	290 ± 150
Total background	287770 ± 570	27580 ± 170	4601 ± 90
Data	287722	27586	4642

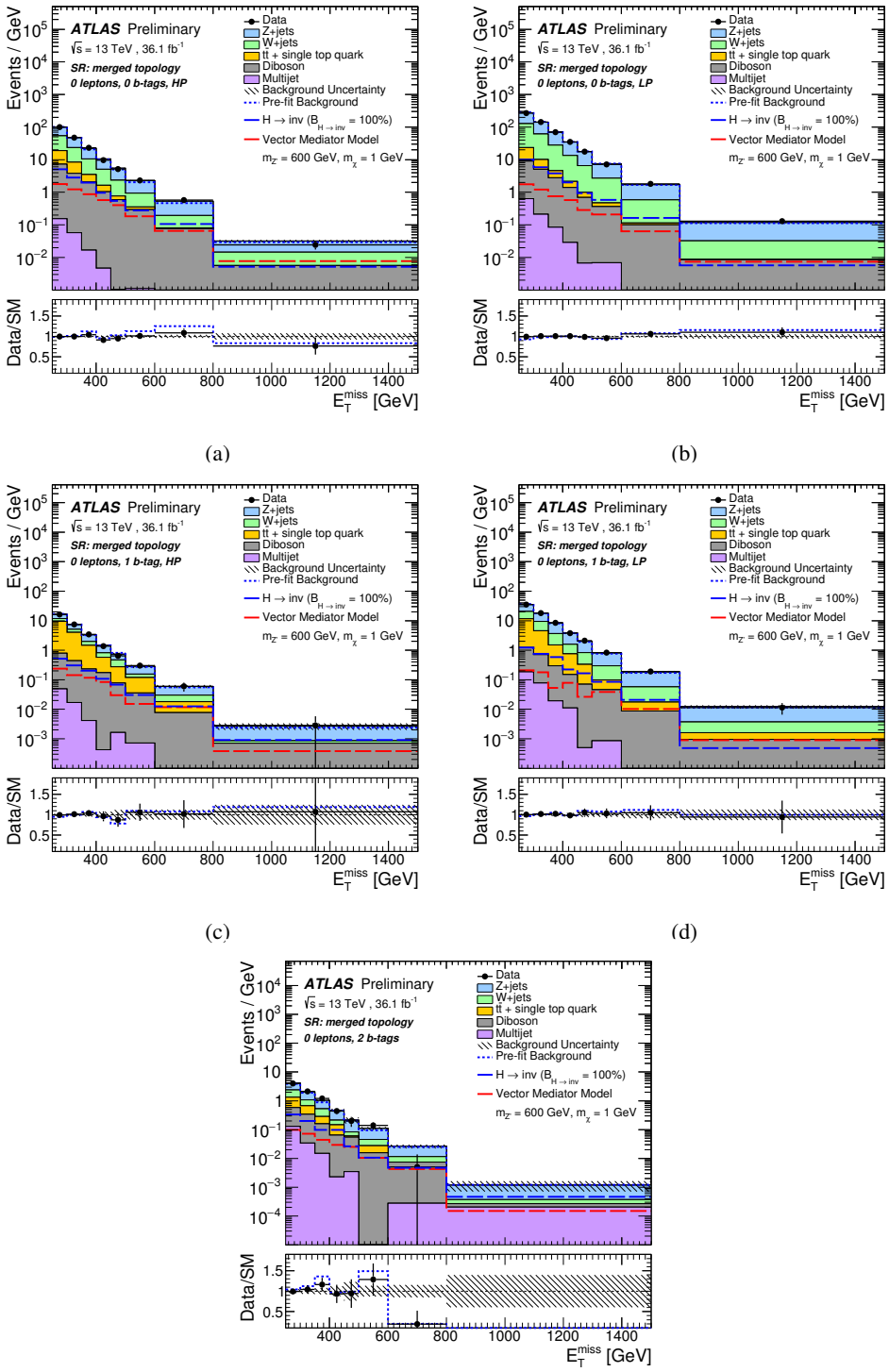

Figure 5: The observed (dots) and expected (coloured histograms) $E_{\mathrm{T}}^{\mathrm{miss}}$ distribution obtained with 36.1 fb^{-1} of data at $\sqrt{s} = 13$ TeV in the mono-W/Z signal region with the merged event topology after the profile likelihood fit, shown separately for the (a) 0b-HP, (b) 0b-LP, (c) 1b-HP, (d) 1b-LP, and (e) 2b-tag event category. The total background contribution before the fit to data is shown as a dotted blue line. The hatched area represents the total background uncertainty. The signal expectation for the simplified vector-mediator model with $m_{\chi} = 1$ GeV and $m_{\mathrm{med}} = 600$ GeV (dashed red line) and for the invisible Higgs boson decays (dashed blue line) is shown for comparison. The inset at the bottom of each plot shows the ratio of the data to the total post-fit (dots) and pre-fit (dotted blue line) background expectation.

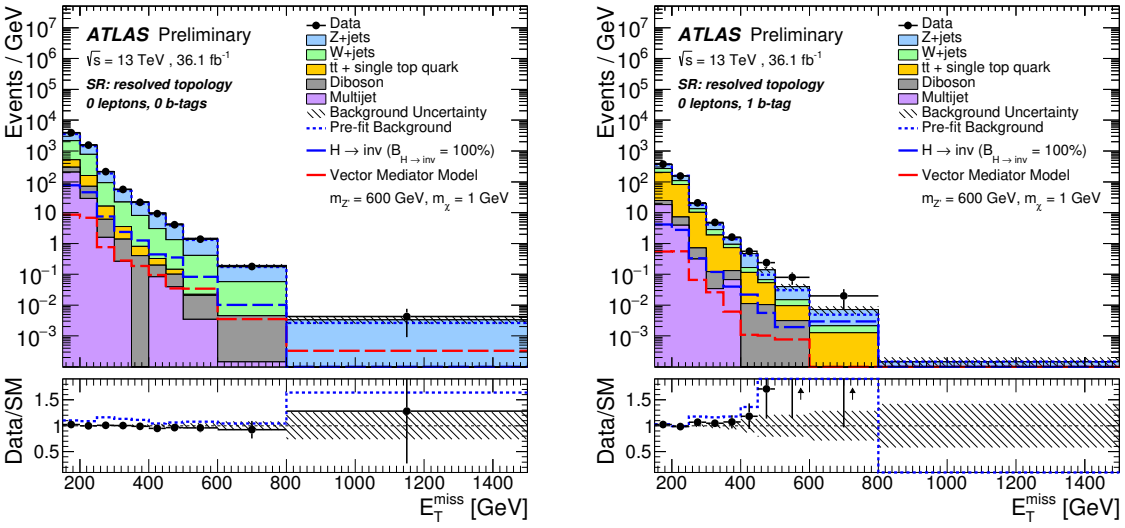

(a)

(b)

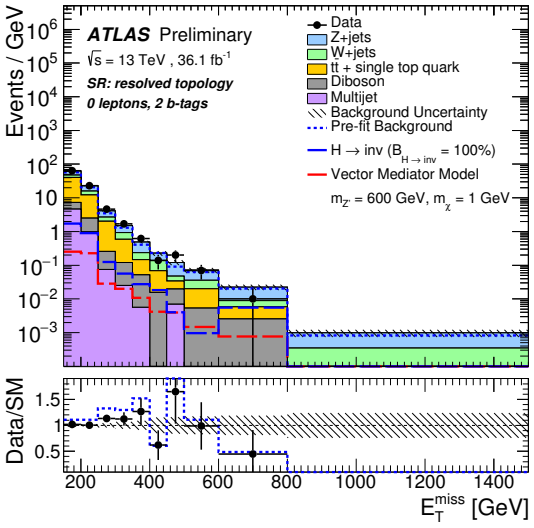

(c)

Figure 6: The observed (dots) and expected (coloured histograms) $E_{\mathrm{T}}^{\mathrm{miss}}$ distribution obtained with 36.1 fb^{-1} of data at $\sqrt{s}$ = 13 TeV in the mono-W/Z signal region with the with the resolved event topology after the profile likelihood fit, shown separately for the (a) 0b-, (b) 1b- and (c) 2b-tag category. The total background contribution before the fit to data is shown as a dotted blue line. The hatched area represents the total background uncertainty. The signal expectation for the simplified vector-mediator model with m_{χ} = 1 GeV and m_{med} = 600 GeV (dashed red line) and for the invisible Higgs boson decays (dashed blue line) is shown for comparison. The inset at the bottom of each plot shows the ratio of the data to the total post-fit (dots) and pre-fit (dotted blue line) background expectation.

Table 4: The expected and observed numbers of events for an integrated luminosity of 36.1 fb^{-1} and $\sqrt{s}$ = 13 TeV, shown separately in each mono-Z' signal region category assuming $m_{Z'}$ = 90 GeV. The background yields and uncertainties are shown after the profile likelihood fit to the data. The quoted background uncertainties include both the statistical and systematic contributions, while the uncertainty on the signal is of statistical nature only. The uncertainties on the total background can be smaller than those on individual components due to anti-correlations of nuisance parameters.

			Merged topology		
Process	0b-HP	0b-LP	1b-HP	1b-LP	2b
Dark fermion, light sector	286 ± 54	125 ± 36	53 ± 23	26 ± 16	52 ± 23
Dark fermion, heavy sector	165 ± 18	71 ± 12	30.9 ± 7.7	18.6 ± 6.0	36.3 ± 8.4
Dark Higgs, light sector	253 ± 25	82 ± 14	37.7 ± 9.6	19.1 ± 6.9	45 ± 11
Dark Higgs, heavy sector	224 ± 14	75.9 ± 8.4	37.5 ± 5.9	21.2 ± 4.4	49.5 ± 6.8
W+jets	2960 ± 170	5180 ± 280	342 ± 52	680 ± 100	120 ± 120
Z+jets	4720 ± 190	7990 ± 310	628 ± 69	1280 ± 140	265 ± 22
$t\bar{t}$	780 ± 110	440 ± 59	646 ± 59	434 ± 49	59 ± 19
Single top-quark	161 ± 15	113 ± 14	93 ± 10	94.1 ± 8.9	17.8 ± 2.8
Diboson	830 ± 130	575 ± 95	129 ± 23	107 ± 18	61 ± 11
Multijet	48 ± 41	21 ± 66	1.2 ± 1.0	5.4 ± 5.1	0.52 ± 0.51
Total background	9498 ± 96	14310 ± 120	1840 ± 37	2600 ± 46	523 ± 19
Data	9516	14282	1845	2628	534

	Resolved topology		
Process	0b	1b	2b
Dark fermion, light sector	2060 ± 150	264 ± 52	228 ± 55
Dark fermion, heavy sector	976 ± 44	121 ± 15	164 ± 18
Dark Higgs, light sector	1206 ± 54	135 ± 18	197 ± 22
Dark Higgs, heavy sector	953 ± 30	112 ± 10	146 ± 12
W+jets	78400 ± 3400	4400 ± 690	1030 ± 190
Z+jets	91700 ± 3800	6970 ± 690	2140 ± 210
$t\bar{t}$	11170 ± 920	10590 ± 530	7760 ± 230
Single top-quark	1200 ± 170	1006 ± 74	602 ± 40
Diboson	6080 ± 930	514 ± 80	337 ± 55
Multijet	14700 ± 2500	1280 ± 540	540 ± 270
Total background	203990 ± 480	24770 ± 220	12400 ± 110
Data	203991	24783	12406

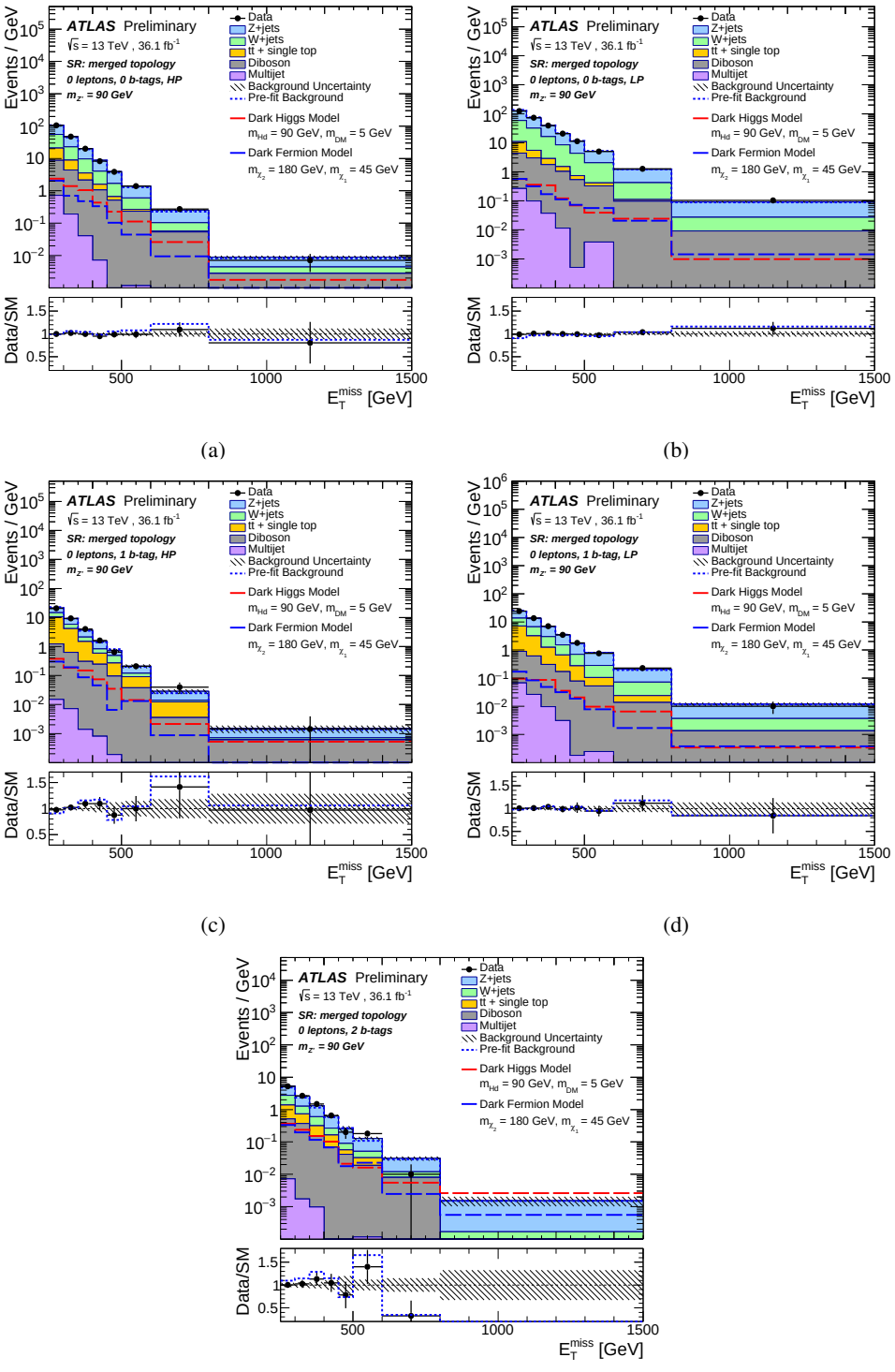

Figure 7: The observed (dots) and expected (coloured histograms) $E_{\mathrm{T}}^{\mathrm{miss}}$ distribution obtained with 36.1 fb^{-1} of data at $\sqrt{s}$ = 13 TeV in the mono-Z' signal region with $m_{Z'}$ = 90 GeV and the merged event topology after the profile likelihood fit, shown separately for the (a) 0b-HP, (b) 0b-LP, (c) 1b-HP, (d) 1b-LP, and (e) 2b-tag event category. The total background contribution before the fit to data is shown as a dotted blue line. The hatched area represents the total background uncertainty. The expectation for the selected dark-Higgs (dashed red line) and dark-fermion (dashed blue line) signal points is shown for comparison. The inset at the bottom of each plot shows the ratio of the data to the total post-fit (dots) and pre-fit (dotted blue line) background expectation.

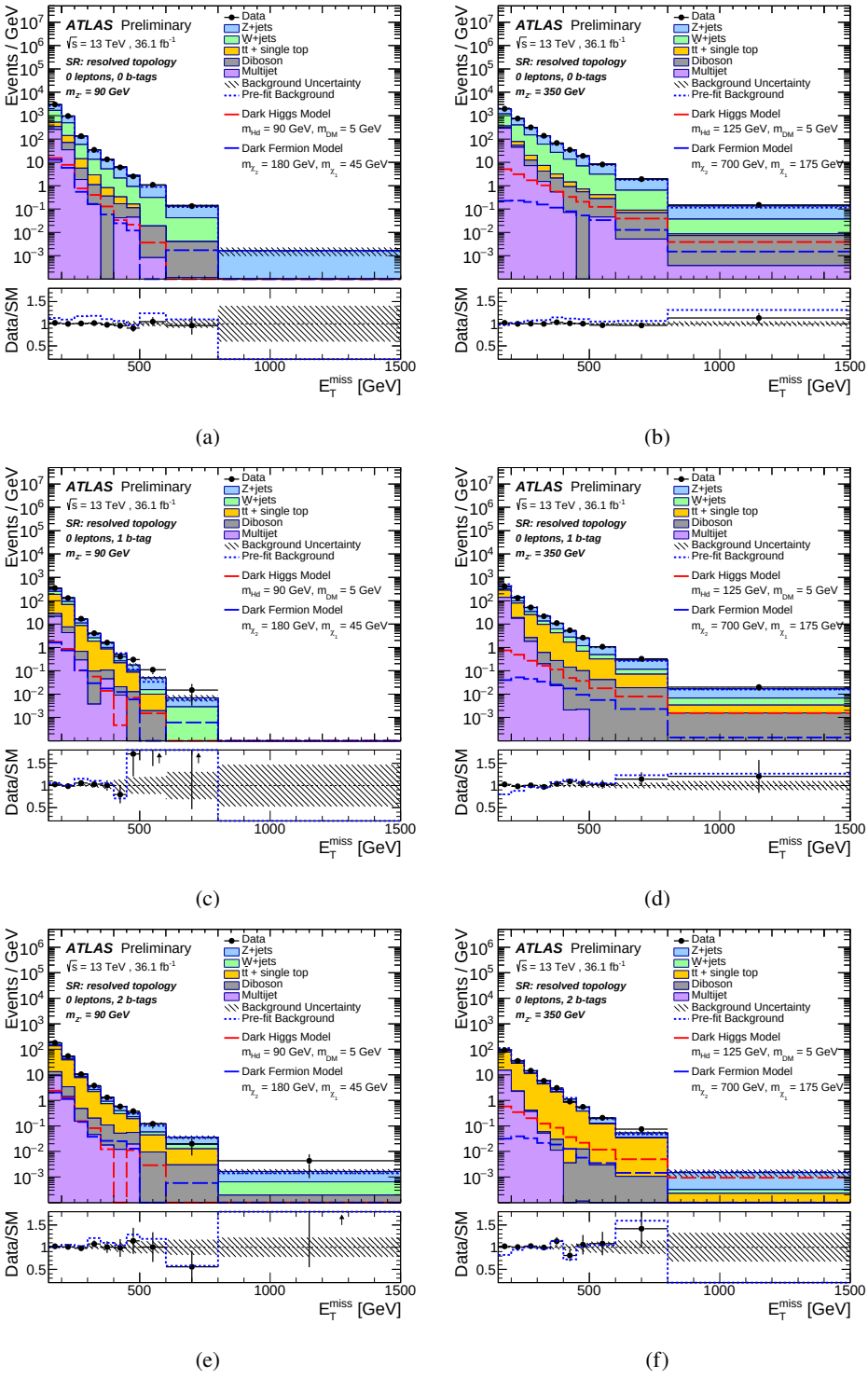

Figure 8: The observed (dots) and expected (coloured histograms) $E_{\mathrm{T}}^{\mathrm{miss}}$ distribution obtained with 36.1 fb^{-1} of data at $\sqrt{s}$ = 13 TeV in the mono-Z' signal region with the resolved event topology after the profile likelihood fit, shown separately for the (a,b) 0b, (c,d) 1b and (e,f) 2b-tag event category. On the left-hand side, the mediator mass of 90 GeV and on the right-hand side of 350 GeV is assumed. The total background contribution before the fit to data is shown as a dotted blue line. The hatched area represents the total background uncertainty. The expectation for the selected dark-Higgs (dashed red line) and dark-fermion (dashed blue line) signal points is shown for comparison. The inset at the bottom of each plot shows the ratio of the data to the total post-fit (dots) and pre-fit (dotted blue line) background expectation.

Table 5: The expected and observed numbers of events for an integrated luminosity of 36.1 fb^{-1} and $\sqrt{s}$ = 13 TeV, shown separately in each mono-Z' signal region category assuming $m_{Z'}$ = 350 GeV. The background yields and uncertainties are shown after the profile likelihood fit to the data. The quoted background uncertainties include both the statistical and systematic contributions, while the uncertainty on the signal is of statistical nature only. The uncertainties on the total background can be smaller than those on individual components due to anti-correlations of nuisance parameters.

	Resolved topology		
Process	$0b$	$1b$	$2b$
Dark fermion, light sector	655 ± 14	104.2 ± 5.8	89.5 ± 5.3
Dark fermion, heavy sector	70.79 ± 0.79	12.45 ± 0.33	9.04 ± 0.28
Dark Higgs, light sector	639 ± 13	96.7 ± 4.9	72.3 ± 4.3
Dark Higgs, heavy sector	118.9 ± 1.4	19.62 ± 0.58	14.24 ± 0.50
W+jets	68300 ± 4300	4270 ± 1100	115 ± 84
Z+jets	72200 ± 3000	7230 ± 800	1160 ± 110
$t\bar{t}$	3900 ± 460	10320 ± 720	4920 ± 140
Single top-quark	752 ± 69	1530 ± 110	466 ± 35
Diboson	2000 ± 340	282 ± 47	14.6 ± 2.8
Multijet	17100 ± 2300	7870 ± 390	880 ± 140
Total background	164310 ± 650	31520 ± 250	7567 ± 85
Data	164386	31465	7597

for any of the signal mass points, both in case of the mono-W/Z and mono-Z' searches. A modified frequentist method with the CL_s formalism [81] is used to set upper limits on the signal strength μ at 95% confidence level for all studied signal models.

In the search for invisible Higgs boson decays, an observed (expected) upper limit of 0.83 ($0.58^{+0.23}_{-0.16}$) is obtained at 95% CL on the the branching ratio $\mathcal{B}_{H\to\text{inv.}}$, assuming the SM production cross sections and combining the contributions from VH, ggH and VBF production modes. The expected limit is a factor of about 1.5 better than the one reached by the previous analysis of Run-1 ATLAS data [6].

In the context of the mono-W/Z simplified vector-mediator signal model, the exclusion limits on the signal strength are shown in Figure 9(a) and translated into limits on the dark matter and mediator masses (see Figure 9(b)). Since only a limited number of signal points have been simulated, an interpolation procedure is employed to obtain the limits on the signal strength at other mass points in the $(m_\chi, m_{Z'})$ parameter plane. For that purpose, all signal processes with the same mediator mass $m_{Z'}$ and different m_χ values are assumed to have similar $(\mathcal{A}\times\varepsilon)_{\text{total}}$ values as in the simulated sample with m_χ = 1 GeV. This was verified to be a reliable approximation for $m_{Z'} > 2m_\chi$. Thus, the expected signal yield at a given mass point $(m_{Z'}, m_\chi)$ only depends on the cross section $\sigma^{(m_{Z'},m_\chi)}_{pp\to Z'\to\chi\chi}$ at that mass point. Under the narrow width approximation, this cross section can be expressed in terms of the cross section $\sigma^{(m_{Z'},m_\chi=1\text{ GeV})}_{pp\to Z'\to\chi\chi}$ and the branching ratio $\mathcal{B}^{m_\chi=1\text{ GeV}}_{Z'\to\chi\chi}$ at the simulated mass point with m_χ = 1 GeV,

$$\sigma^{(m_{Z'},m_\chi)}_{pp\to Z'\to\chi\chi} = \sigma^{(m_{Z'},m_\chi=1\text{ GeV})}_{pp\to Z'\to\chi\chi}\cdot\frac{\mathcal{B}^{m_\chi}_{Z'\to\chi\chi}}{\mathcal{B}^{m_\chi=1\text{ GeV}}_{Z'\to\chi\chi}},$$

Source of uncertainty	Uncertainty on μ =1 [%]				
	Vector mediator, $m_{Z'}$ =		$H \rightarrow$invisible	Dark fermion, $m_{Z'}$ =	
	200 GeV	600 GeV	($\mathcal{B}_{H\rightarrow\text{inv.}}$ = 100%)	90 GeV	300 GeV
Large-R jets	9	20	17	23	-
Small-R jets	3	8	7	13	6
Electrons	4	9	6	7	8
Muons	6	7	7	15	14
$E_{\text{T}}^{\text{miss}}$	1	4	3	4	3
b-tagging (track jets)	4	4	4	8	-
b-tagging (small-R jets)	2	4	2	5	11
Luminosity	3	4	3	4	4
Multijet normalization	7	11	11	13	11
Diboson normalization	5	11	6	3	1
Z+jets normalization	5	9	4	15	12
W+jets normalization	3	4	2	8	7
$t\bar{t}$ normalization	3	1	0.3	8	6
Signal modeling	7	9	20	-	-
V+jets modeling	4	10	4	7	13
$t\bar{t}$ modeling	2	4	3	10	8
V+jets flavor composition	1	3	3	4	3
Diboson modeling	1	2	2	1	0.3
Background MC stat.	10	18	14	20	19
Total syst.	21	40	38	45	42
Data stat.	7	21	5	14	18
Total	22	45	39	47	47

Table 6: Breakdown of expected signal strength uncertainties for several mono-W/Z and mono-Z' signal models, obtained for an integrated luminosity of 36.1 fb^{-1} and $\sqrt{s}$ = 13 TeV. A dark matter mass of 1 GeV is used in case of the two vector-mediator signals. Each systematic uncertainty contribution is provided as the quadratic difference between the total uncertainty and the uncertainty obtained by neglecting the systematic uncertainty in question. Only the largest systematic uncertainties are shown.

where the value of the branching ratio $\mathcal{B}^{m_\chi}_{Z'\to\chi\chi}$ is fully defined by the values of model parameters g_{DM}, g_{SM}, m_χ and $m_{Z'}$. Vector-mediator masses $m_{Z'}$ of up to 650 GeV are excluded at 95% CL for dark matter masses m_χ of up to 250 GeV, agreeing well with the expected exclusion of the Z' masses of up to 700 GeV for m_χ of up to 230 GeV. The reported expected limits are improved by 15% – 30%, depending on the DM mass, compared to the analysis presented in Ref. [1].

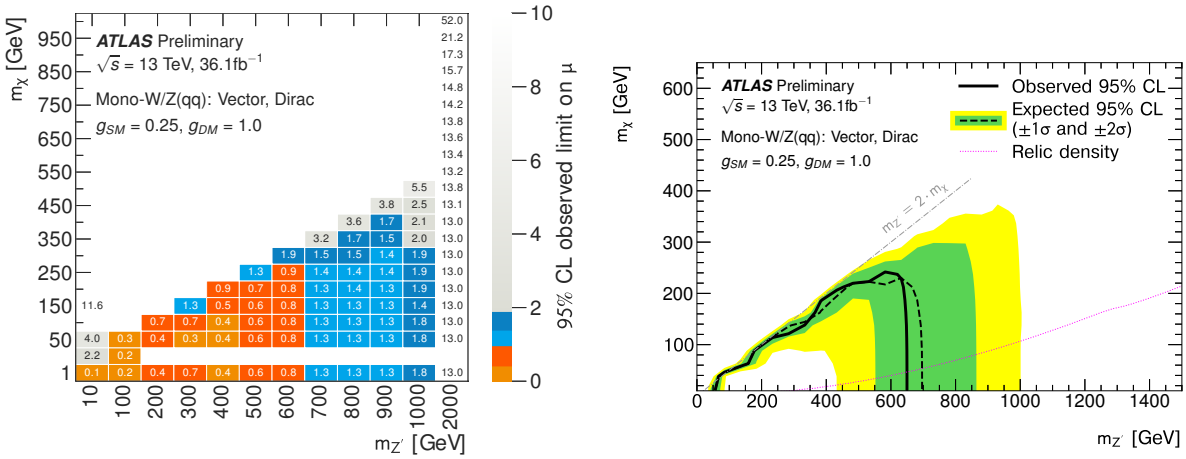

(a) (b)

Figure 9: (a) Observed upper limits on the signal strength μ at 95% CL in the studied grid of the DM and mediator particle masses, (m_χ, $m_{Z'}$), for the combined mono-W and mono-Z search in the frame of the simplified vector-mediator model with Dirac DM particles and couplings $g_{\mathrm{SM}} = 0.25$ and $g_{\mathrm{DM}} = 1$. There are no interpolated points and thus no limit values listed for the mass point (m_χ = 100 GeV, $m_{Z'}$ = 10 GeV) and in the parameter region (m_χ = 10 GeV, $m_{Z'}$ = 200-2000 GeV). (b) The corresponding exclusion contours at 95% CL. The black solid (dashed) curve shows the median of the observed (expected) limit. The dotted magenta curve corresponds to the set of points for which the expected relic density is consistent with the WMAP [82] and Planck [83] measurements ($\Omega h^2 = 0.12$), as computed with MadDM [84]. The region on the right of the curve corresponds to higher predicted relic abundance than these measurements.

In addition to the interpretation of the mono-W/Z search in terms of the simplified vector-mediator model and invisible Higgs boson decays, the analysis results are also expressed in terms of generic CL_s upper limits at 95% CL on the allowed visible cross-section σ_{vis} of potential $W+\mathrm{DM}$ or $Z+\mathrm{DM}$ production. The limits for these two processes are evaluated separately to allow for more flexibility in terms of possible reinterpretations, as new models might prefer one of these two final states. While the event selection and categorization is the same as described in Section 6, i.e. including the b-tagging and mass window requirements, the exclusion limits are provided in the fiducial region that is defined by applying all signal region selection criteria except for the requirements on m_{jj} or m_J and the b-tagging multiplicity. With this definition, the exclusion limits on σ_{vis} apply to any processes which are characterized by a generic back-to-back topology with a W/Z boson recoiling against $E_{\mathrm{T}}^{\mathrm{miss}}$ from weakly interacting particles such as DM. The limits on σ_{vis} are given as a function of the $E_{\mathrm{T}}^{\mathrm{miss}}$ variable in order to avoid any additional model-dependent assumptions on the $E_{\mathrm{T}}^{\mathrm{miss}}$ distribution. Hence, the $E_{\mathrm{T}}^{\mathrm{miss}}$ bins in the 0-lepton region are treated independently of each other in the statistical interpretation of the data. The bins are joined into a smaller number of bins at $E_{\mathrm{T}}^{\mathrm{miss}} > 300$ GeV to improve the statistics in the per-bin analysis. In all other aspects, the approach is identical to the mono-W/Z analysis described above. The mono-W/Z vector-mediator signal samples are used as a benchmark model to estimate the residual dependence of

the σ_{vis} limits on the kinematic properties of events within a given $E_{\text{T}}^{\text{miss}}$ range and on the b-tagging multiplicity. For this, a wide range of $(m_{Z'}, m_{\chi})$ model parameters that yield a sizeable contribution of at least 500 simulated MC events in a given $E_{\text{T}}^{\text{miss}}$ range is considered. Corresponding variations of 15-50% (25-50%) in the expected limits on $\sigma_{\text{vis, W+DM}}$ ($\sigma_{\text{vis, Z+DM}}$) are found. The weakest σ_{vis} limit is quoted in a given range of the reconstructed $E_{\text{T}}^{\text{miss}}$ in order to minimize the dependence on a benchmark model. The observed and expected limits on σ_{vis} in each studied $E_{\text{T}}^{\text{miss}}$ range are shown in Figure 10, with the numerical values summarized in Tables 7 and 8. As a general trend, the limits on the Z + DM production are somewhat stronger than those on W + DM since the former significantly contribute to the $2b$ category that features the highest sensitivity due to having the lowest SM backgrounds.

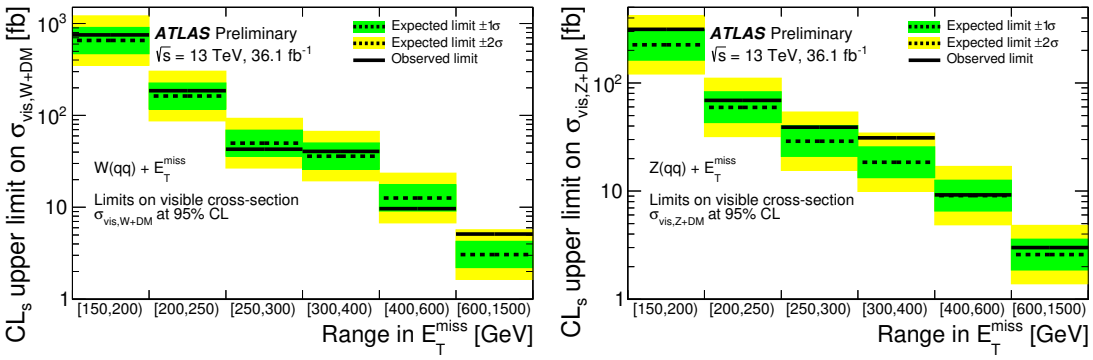

Figure 10: Upper limits at 95% CL on the visible cross-section $\sigma_{\text{vis, W+DM}}$ (left) and $\sigma_{\text{vis, Z+DM}}$ (right) in the six $E_{\text{T}}^{\text{miss}}$ regions, after all selections, but inclusive in the b-tag multiplicity and the W/Z candidate mass m_{jj}/m_J. The observed limits (solid line) are consistent with the expectations under the SM-only hypothesis (dashed line) within uncertainties (filled bands).

$E_{\text{T}}^{\text{miss}}$ range [GeV]	Upper limit at 95% CL [fb] $\sigma_{\text{vis}}^{\text{obs}}$	$\sigma_{\text{vis}}^{\text{exp}}$	-1σ	$+1\sigma$	$A \times \varepsilon$
W+DM, $W \to q'q$					
[150, 200)	750	650	470	910	20%
[200, 250)	185	163	117	226	20%
[250, 300)	43	50	36	69	30%
[300, 400)	41	36	26	50	45%
[400, 600)	9.7	12.6	9.1	17.6	55%
[600, 1500)	5.1	3.1	2.2	4.3	55%

Table 7: The observed and expected exclusion limit at 95% CL on σ_{vis} of the W + DM production for an integrated luminosity of 36.1 fb^{-1} and $\sqrt{s}$ = 13 TeV, together with the corresponding product of acceptance times efficiency $(A \times \varepsilon)$ for different regions of $E_{\text{T}}^{\text{miss}}$.

The observable σ_{vis} can be interpreted as

$$\sigma_{\text{vis, W+DM}}(E_{\text{T}}^{\text{miss}}) \equiv \sigma_{W\text{+DM}}(E_{\text{T}}^{\text{miss}}) \times \mathcal{B}_{W\to q'q} \times (A \times \varepsilon)(E_{\text{T}}^{\text{miss}}) \quad \text{for } W \text{ + DM events}, \tag{1}$$

$$\sigma_{\text{vis, Z+DM}}(E_{\text{T}}^{\text{miss}}) \equiv \sigma_{Z\text{+DM}}(E_{\text{T}}^{\text{miss}}) \times \mathcal{B}_{Z\to q\bar{q}} \times (A \times \varepsilon)(E_{\text{T}}^{\text{miss}}) \quad \text{for } Z \text{ + DM events}, \tag{2}$$

where $\sigma_{W\text{+DM}}$ ($\sigma_{Z\text{+DM}}$) is the production cross-section of W + DM (Z + DM) events in a given $E_{\text{T}}^{\text{miss}}$ range, $\mathcal{B}_{W\to q'q}$ ($\mathcal{B}_{Z\to q\bar{q}}$) is the branching ratio for the hadronic W (Z) boson decay, and $(A \times \varepsilon)(E_{\text{T}}^{\text{miss}})$

$E_{\mathrm{T}}^{\mathrm{miss}}$ range [GeV]	Upper limit at 95% CL [fb] $\sigma_{\mathrm{vis}}^{\mathrm{obs}}$	$\sigma_{\mathrm{vis}}^{\mathrm{exp}}$	-1σ	$+1\sigma$	$A \times \varepsilon$
Z+DM, $Z \to q\bar{q}$					
[150, 200)	313	225	162	314	20%
[200, 250)	69	60	43	83	20%
[250, 300)	39	29	21	40	30%
[300, 400)	31.1	18.5	13.3	25.7	45%
[400, 600)	9.2	9.1	6.5	12.6	50%
[600, 1500)	3.0	2.6	1.9	3.6	55%

Table 8: The observed and expected exclusion limit at 95% CL on σ_{vis} of the Z + DM production for an integrated luminosity of 36.1 fb^{-1} and $\sqrt{s}$ = 13 TeV, together with the corresponding product of acceptance times efficiency ($A \times \varepsilon$) for different regions of $E_{\mathrm{T}}^{\mathrm{miss}}$.

is the product of the kinematic acceptance and the experimental efficiency. This product represents the fraction of simulated W/Z + DM events in a given $E_{\mathrm{T}}^{\mathrm{miss}}$ range at parton level[2] that fall into the same $E_{\mathrm{T}}^{\mathrm{miss}}$ range at detector level after reconstruction, and pass the event selection criteria applied to determine σ_{vis}. The latter do not include the requirements on m_{jj}/m_J or b-tagging to allow for a generic interpretation. The product $(A \times \varepsilon)(E_{\mathrm{T}}^{\mathrm{miss}})$ in a given $E_{\mathrm{T}}^{\mathrm{miss}}$ range has been evaluated for each simulated vector-mediator signal and the lowest of these values, rounded down in steps of 5%, has been taken for the limit calculation. The values obtained for each $E_{\mathrm{T}}^{\mathrm{miss}}$ range are listed in Tables 7 and 8.

For the mono-Z' models, the upper limits on the cross section at 95% CL are shown in Figure 11 as a function of the mediator mass for both the dark-fermion and dark-Higgs models in the light and heavy dark-sector mass scenarios. The largest excess of the data above the expectation, corresponding to a local significance of 3σ, is observed for a hypothesized signal at $m_{Z'}$ = 350 GeV within the dark fermion model in the heavy dark-sector scenario. Taking into account the look-elsewhere effect [85] with respect to the 19 overlapping mass windows examined in the mono-Z' search, the excess corresponds to a global significance of 2.2σ. Cross section exclusions limits for the dark-fermion model (dark-Higgs model) in the light and the heavy dark-sector scenario are in the range of 0.68 – 27 pb and 0.066 – 9.8 pb (0.80 – 5.5 pb and 0.064 – 2.4 pb), respectively, for Z' masses between 80 and 500 GeV. The corresponding observed and expected upper limits on the coupling g_{SM} are shown in Figure 12, assuming g_{DM} = 1.

[2] At parton level, $E_{\mathrm{T}}^{\mathrm{miss}}$ is defined as the negative vector sum of momenta of neutrinos and DM particles in the transverse detector plane.

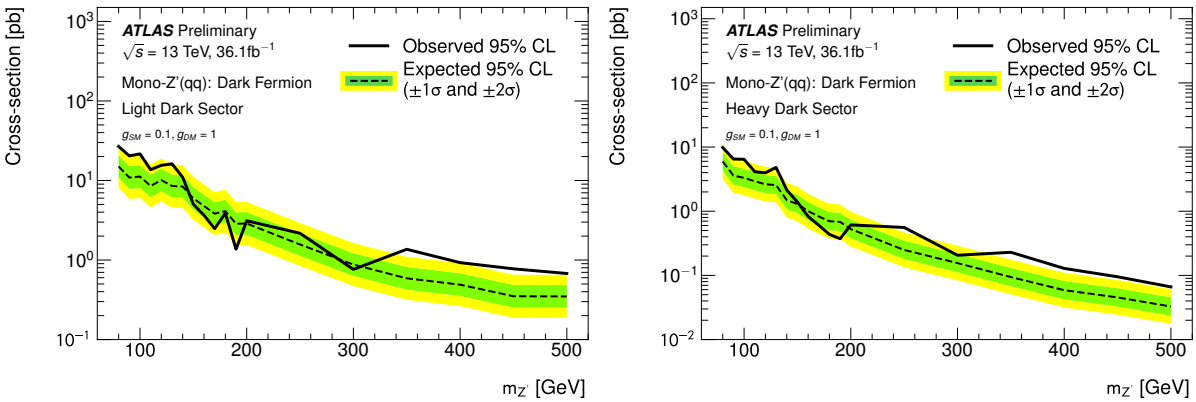

(a)

(b)

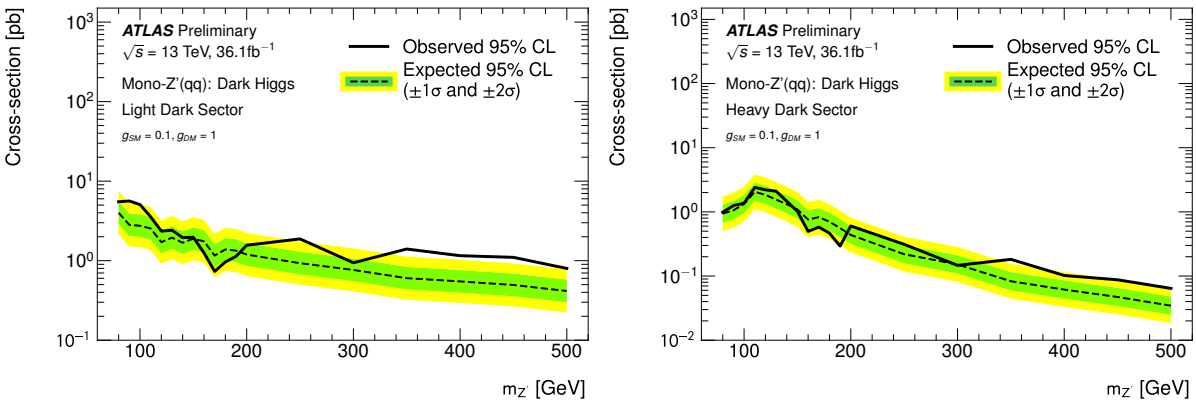

(c)

(d)

Figure 11: Upper limits at 95% CL on the cross section in mono-Z' models as a function of the mediator mass for the dark fermion model in the (a) light and (b) heavy dark-sector scenario, as well as the dark Higgs model in the (c) light and (d) heavy dark-sector scenario.

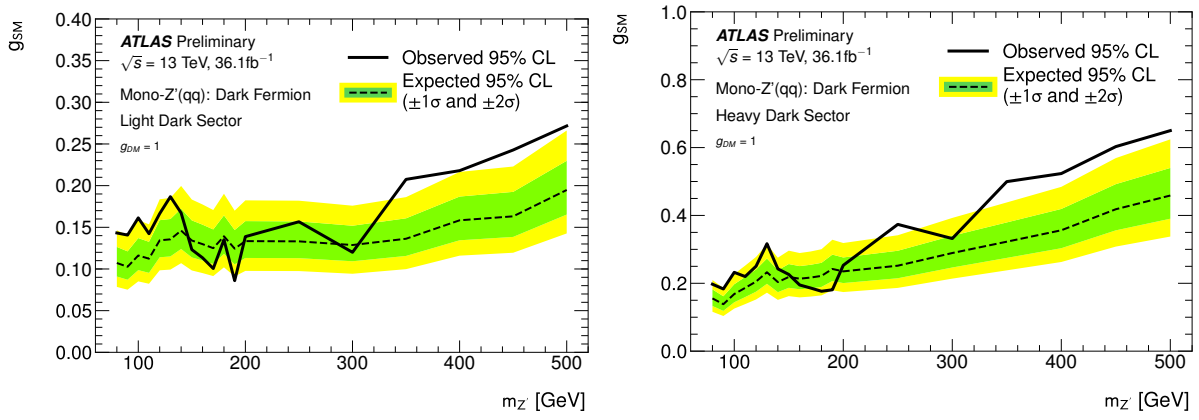

(a)

(b)

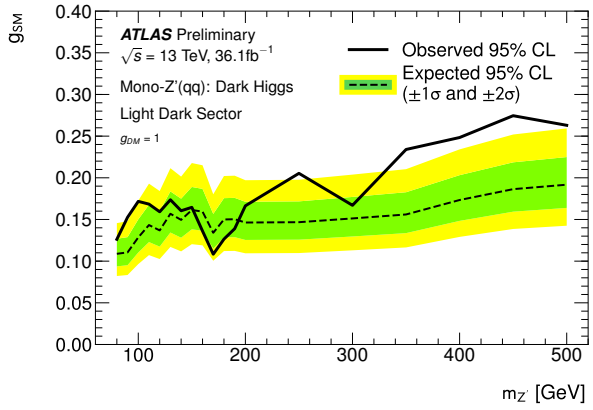

(c)

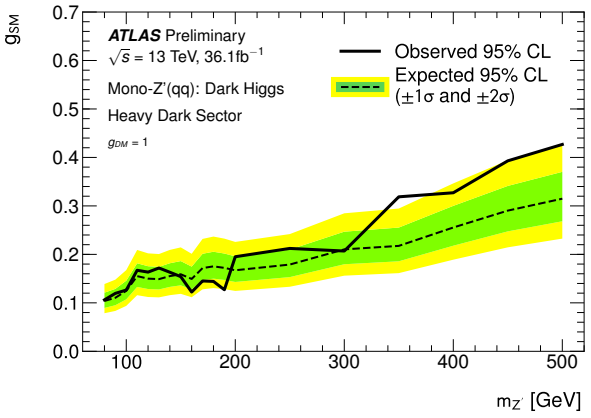

(d)

Figure 12: Upper limits at 95% CL on the product of couplings $g_{\mathrm{SM}}\, g_{\mathrm{DM}}$ in mono-Z' models as a function of the mediator mass for the (a) dark fermion model in the light and (b) heavy dark-sector scenario, as well as the (c) dark Higgs model in the light and (d) heavy dark-sector scenario.

10 Summary

A search for dark matter has been performed in events having a large-R jet or a pair of small-R jets compatible with a hadronic W or Z boson decay and large $E_{\mathrm{T}}^{\mathrm{miss}}$. In addition, the as of yet unexplored hypothesis of a new vector boson Z' produced in association with dark matter is considered. This search is using the ATLAS dataset containing 36.1 fb^{-1} of $\sqrt{s}$ = 13 TeV pp collisions collected in year 2015 and 2016, which improves on the previous searches with a larger dataset and further optimization of the selection and signal region definitions. The results are in agreement with the SM predictions and are translated into exclusion limits on DM-pair production.

Two simplified models are considered to describe DM production in the mono-W/Z final state. For the *simplified vector-mediator model* in which the DM is produced via an s-channel exchange of a vector mediator Z', masses $m_{Z'}$ of up to 650 GeV are excluded for dark matter masses m_{χ} of up to 250 GeV (assuming $g_{\mathrm{SM}} = 0.25$ and $g_{\mathrm{DM}} = 1.0$). This agrees well with the expected exclusion of the $m_{Z'}$ values of up to 700 GeV for m_{χ} of up to 230 GeV. Limits are also placed on the visible cross-section of non-SM events with large $E_{\mathrm{T}}^{\mathrm{miss}}$ and a W or a Z boson without extra model assumptions. In the search for *invisible Higgs boson decays*, an upper limit of 0.83 is observed at 95% CL on the branching ratio $\mathcal{B}_{H\to\mathrm{inv.}}$, while the corresponding expected limit is 0.58.

Two additional signal models are taken into account for DM production in association with the non-SM vector boson Z'. In the *dark-fermion model*, the intermediate Z' boson couples to a heavier dark-sector fermion χ_2 as well as the lighter DM candidate fermion χ_1. In the *dark-Higgs model*, a dark-sector Higgs boson which decays to $\chi\chi$ pair is radiated from the Z' boson. For coupling values of $g_{\mathrm{SM}} = 0.1$ and $g_{\mathrm{DM}} = 1.0$, two different choices of masses m_{χ_2} and m_{h_D} of intermediate dark-sector particles are considered. Cross section exclusions limits for the dark-fermion model in the light and heavy dark sector scenarios are in the range of 0.68 – 27 pb and 0.066 – 9.8 pb, respectively, for Z' masses between 80 and 500 GeV. The corresponding limits for the dark-Higgs model in the light and heavy dark sector scenario are 0.80 – 5.5 pb and 0.064 – 2.4 pb, respectively.

References

[1] ATLAS Collaboration, *Search for dark matter produced in association with a hadronically decaying vector boson in pp collisions at* $\sqrt{s} = 13$ *TeV with the ATLAS detector*, Phys. Lett. B **763** (2016) 251, arXiv: 1608.02372 [hep-ex].

[2] CMS Collaboration, *Search for new physics in final states with an energetic jet or a hadronically decaying W or Z boson and transverse momentum imbalance at* $\sqrt{s} = 13$ *TeV*, submitted to Phys. Rev. D. (2017), arXiv: 1712.02345 [hep-ex].

[3] ATLAS Collaboration, *Search for dark matter in events with a hadronically decaying W or Z boson and missing transverse momentum in pp collisions at* $\sqrt{s} = 8$ *TeV with the ATLAS detector*, Phys. Rev. Lett. **112** (2014) 041802, arXiv: 1309.4017 [hep-ex].

[4] CMS Collaboration, *Search for dark matter in proton–proton collisions at* 8 *TeV with missing transverse momentum and vector boson tagged jets*, JHEP **12** (2016) 083, arXiv: 1607.05764 [hep-ex].

[5] ATLAS Collaboration, *Constraints on new phenomena via Higgs boson couplings and invisible decays with the ATLAS detector*, JHEP **11** (2015) 206, arXiv: 1509.00672 [hep-ex].

[6] ATLAS Collaboration, *Search for invisible decays of the Higgs boson produced in association with a hadronically decaying vector boson in pp collisions at* $\sqrt{s} = 8$ *TeV with the ATLAS detector*, Eur. Phys. J. C **75** (2015) 337, arXiv: 1504.04324 [hep-ex].

[7] CMS Collaboration, *Search for invisible decays of Higgs bosons in the vector boson fusion and associated ZH production modes*, Eur. Phys. J. C **74** (2014) 2980, arXiv: 1404.1344 [hep-ex].

[8] LHC Higgs Cross Section Working Group, D. de Florian et al., *Handbook of LHC Higgs Cross Sections: 4. Deciphering the nature of the Higgs sector*, CERN-2017-002-M (CERN, Geneva, 2016), arXiv: 1610.07922 [hep-ph].

[9] I. Antoniadis, M. Tuckmantel and F. Zwirner, *Phenomenology of a leptonic goldstino and invisible Higgs boson decays*, Nucl. Phys. B **707** (2005) 215, arXiv: hep-ph/0410165.

[10] N. Arkani-Hamed, S. Dimopoulos, G. Dvali and J. March-Russell, *Neutrino masses from large extra dimensions*, Phys. Rev. D **65** (2002) 024032, arXiv: hep-ph/9811448.

[11] A. Datta, K. Huitu, J. Laamanen and B. Mukhopadhyaya, *Invisible Higgs in theories of large extra dimensions*, Phys. Rev. D **70** (2004) 075003, arXiv: hep-ph/0404056.

[12] S. Kanemura, S. Matsumoto, T. Nabeshima and N. Okada, *Can WIMP dark matter overcome the nightmare scenario?*, Phys. Rev. D **82** (2010) 055026, arXiv: 1005.5651 [hep-ph].

[13] A. Djouadi, O. Lebedev, Y. Mambrini and J. Quevillon, *Implications of LHC searches for Higgs-portal dark matter*, Phys. Lett. B **709** (2012) 65, arXiv: 1112.3299 [hep-ph].

[14] CMS Collaboration, *Searches for invisible decays of the Higgs boson in pp collisions at* $\sqrt{s} = 7, 8$, *and* 13 *TeV*, JHEP **02** (2017) 135, arXiv: 1610.09218 [hep-ex].

[15] M. Autran, K. Bauer, T. Lin and D. Whiteson,
Searches for dark matter in events with a resonance and missing transverse energy,
Phys. Rev. **D92** (2015) 035007, arXiv: 1504.01386 [hep-ph].

[16] ATLAS Collaboration, *The ATLAS Experiment at the CERN Large Hadron Collider*,
JINST **3** (2008) S08003.

[17] ATLAS Collaboration, *ATLAS Insertable B-Layer Technical Design Report*,
CERN-LHCC-2010-013, ATLAS-TDR-019, 2010,
URL: https://cds.cern.ch/record/1291633.

[18] *ATLAS Insertable B-Layer Technical Design Report Addendum*,
tech. rep. CERN-LHCC-2012-009. ATLAS-TDR-19-ADD-1,
Addendum to CERN-LHCC-2010-013, ATLAS-TDR-019, 2012,
URL: https://cds.cern.ch/record/1451888.

[19] O. Buchmueller, M. J. Dolan, S. A. Malik and C. McCabe, *Characterising dark matter searches at colliders and direct detection experiments: Vector mediators*, JHEP **01** (2015) 037,
arXiv: 1407.8257 [hep-ph].

[20] D. Abercrombie et al., *Dark Matter Benchmark Models for Early LHC Run-2 Searches: Report of the ATLAS/CMS Dark Matter Forum*, (2015), arXiv: 1507.00966 [hep-ex].

[21] S. Agostinelli et al., *GEANT4: A Simulation toolkit*, Nucl. Instrum. Meth. A **506** (2003) 250.

[22] T. Sjostrand, S. Mrenna and P. Z. Skands, *A Brief Introduction to PYTHIA 8.1*,
Comput. Phys. Commun. **178** (2008) 852, arXiv: 0710.3820 [hep-ph].

[23] ATLAS Collaboration, *Summary of ATLAS Pythia 8 tunes*, ATL-PHYS-PUB-2012-003, 2012,
URL: https://cds.cern.ch/record/1474107.

[24] A. Martin, W. Stirling, R. Thorne and G. Watt, *Parton distributions for the LHC*,
Eur. Phys. J. C **63** (2009) 189, arXiv: 0901.0002 [hep-ph].

[25] J. Alwall et al., *The automated computation of tree-level and next-to-leading order differential cross sections, and their matching to parton shower simulations*, JHEP **07** (2014) 079,
arXiv: 1405.0301 [hep-ph].

[26] ATLAS Collaboration, *ATLAS Pythia 8 tunes to 7 TeV data*, ATL-PHYS-PUB-2014-021, 2014,
URL: https://cds.cern.ch/record/1966419.

[27] R. D. Ball et al., *Parton distributions for the LHC Run II*, JHEP **04** (2015) 040,
arXiv: 1410.8849 [hep-ph].

[28] A. Albert et al., *Recommendations of the LHC Dark Matter Working Group: Comparing LHC searches for heavy mediators of dark matter production in visible and invisible decay channels*,
(2017), arXiv: 1703.05703 [hep-ex].

[29] ATLAS Collaboration,
Search for light resonances decaying to boosted quark pairs and produced in association with a photon or a jet in proton-proton collisions at $\sqrt{s} = 13$ *TeV with the ATLAS detector*,
submitted to Phys. Lett. B (2018), arXiv: 1801.08769 [hep-ex].

[30] CMS Collaboration, *Search for low mass vector resonances decaying into quark-antiquark pairs in proton–proton collisions at* $\sqrt{s} = 13$ *TeV*, JHEP **01** (2017) 097, arXiv: 1710.00159 [hep-ex].

[31] ATLAS Collaboration, *Search for new phenomena in final states with an energetic jet and large missing transverse momentum in pp collisions at* $\sqrt{s} = 13$ *TeV using the ATLAS detector*, Phys. Rev. D **94** (2016) 032005, arXiv: 1604.07773 [hep-ex].

[32] CMS Collaboration, *Search for dijet resonances in proton–proton collisions at* $\sqrt{s} = 13$ *TeV and constraints on dark matter and other models*, Phys. Lett. B **769** (2017) 520, arXiv: 1611.03568 [hep-ex].

[33] ATLAS Collaboration, *Measurement of inclusive and differential cross sections in the* $H \to ZZ^* \to 4\ell$ *decay channel in pp collisions at* $\sqrt{s} = 13$ *TeV with the ATLAS detector*, JHEP **10** (2017) 132, arXiv: 1708.02810 [hep-ex].

[34] ATLAS Collaboration, *Evidence for the* $H \to b\bar{b}$ *decay with the ATLAS detector*, JHEP **12** (2017) 024, arXiv: 1708.03299 [hep-ex].

[35] T. Gleisberg et al., *Event generation with SHERPA 1.1*, JHEP **02** (2009) 007, arXiv: 0811.4622 [hep-ph].

[36] T. Gleisberg and S. Hoeche, *Comix, a new matrix element generator*, JHEP **12** (2008) 039, arXiv: 0808.3674 [hep-ph].

[37] F. Cascioli, P. Maierhofer and S. Pozzorini, *Scattering Amplitudes with Open Loops*, Phys. Rev. Lett. **108** (2012) 111601, arXiv: 1111.5206 [hep-ph].

[38] S. Schumann and F. Krauss, *A Parton shower algorithm based on Catani-Seymour dipole factorisation*, JHEP **03** (2008) 038, arXiv: 0709.1027 [hep-ph].

[39] S. Hoeche, F. Krauss, M. Schönherr and F. Siegert, *QCD matrix elements + parton showers: The NLO case*, JHEP **04** (2013) 027, arXiv: 1207.5030 [hep-ph].

[40] K. Melnikov and F. Petriello, *Electroweak gauge boson production at hadron colliders through* $O(\alpha_s^2)$, Phys. Rev. D **74** (2006) 114017, arXiv: hep-ph/0609070.

[41] P. Nason, *A New method for combining NLO QCD with shower Monte Carlo algorithms*, JHEP **11** (2004) 040, arXiv: hep-ph/0409146.

[42] S. Frixione, P. Nason and C. Oleari, *Matching NLO QCD computations with Parton Shower simulations: the POWHEG method*, JHEP **11** (2007) 070, arXiv: 0709.2092 [hep-ph].

[43] S. Alioli, P. Nason, C. Oleari and E. Re, *A general framework for implementing NLO calculations in shower Monte Carlo programs: the POWHEG BOX*, JHEP **06** (2010) 043, arXiv: 1002.2581 [hep-ph].

[44] P. Artoisenet, R. Frederix, O. Mattelaer and R. Rietkerk, *Automatic spin-entangled decays of heavy resonances in Monte Carlo simulations*, JHEP **03** (2013) 015, arXiv: 1212.3460 [hep-ph].

[45] T. Sjostrand, S. Mrenna and P. Z. Skands, *PYTHIA 6.4 Physics and Manual*, JHEP **05** (2006) 026, arXiv: hep-ph/0603175.

[46] J. Pumplin et al., *New generation of parton distributions with uncertainties from global QCD analysis*, JHEP **07** (2002) 012, arXiv: hep-ph/0201195.

[47] P. Z. Skands, *Tuning Monte Carlo Generators: The Perugia Tunes*, Phys. Rev. D **82** (2010) 074018, arXiv: 1005.3457 [hep-ph].

[48] D. J. Lange, *The EvtGen particle decay simulation package*, Nucl. Instrum. Meth. A **462** (2001) 152.

[49] M. Czakon, P. Fiedler and A. Mitov, *Total Top-Quark Pair-Production Cross Section at Hadron Colliders Through $O(a\frac{4}{S})$*, Phys. Rev. Lett. **110** (2013) 252004, arXiv: 1303.6254 [hep-ph].

[50] T. Stelzer, Z. Sullivan and S. Willenbrock, *Single-top-quark production via W-gluon fusion at next-to-leading order*, Phys. Rev. D **56** (1997) 5919.

[51] T. Stelzer, Z. Sullivan and S. Willenbrock, *Single top quark production at hadron colliders*, Phys. Rev. **D58** (1998) 094021, arXiv: hep-ph/9807340.

[52] M. C. Smith and S. Willenbrock, *QCD and Yukawa corrections to single top quark production via $q\bar{q} \to t\bar{b}$*, Phys. Rev. **D54** (1996) 6696, arXiv: hep-ph/9604223.

[53] N. Kidonakis, 'Top Quark Production', *Proceedings, Helmholtz International Summer School on Physics of Heavy Quarks and Hadrons (HQ 2013): JINR, Dubna, Russia, July 15-28, 2013*, 2014 139, arXiv: 1311.0283 [hep-ph].

[54] C. Patrignani et al. (Particle Data Group), *The review of particle physics (2017)*, Chin. Phys. C **40** (2016) 100001 and 2017 update.

[55] ATLAS Collaboration, *Topological cell clustering in the ATLAS calorimeters and its performance in LHC Run 1*, Eur. Phys. J. C **77** (2017) 490, arXiv: 1603.02934 [hep-ex].

[56] M. Cacciari, G. P. Salam and G. Soyez, *The anti-k_T jet clustering algorithm*, JHEP **04** (2008) 063, arXiv: 0802.1189 [hep-ph].

[57] ATLAS Collaboration, *Tagging and suppression of pileup jets with the ATLAS detector*, ATLAS-CONF-2014-018, 2014, URL: https://cds.cern.ch/record/1700870.

[58] ATLAS Collaboration, *Jet energy scale measurements and their systematic uncertainties in proton–proton collisions at $\sqrt{s}$ = 13 TeV with the ATLAS detector*, Phys. Rev. D **96** (2017) 072002, arXiv: 1703.09665 [hep-ex].

[59] ATLAS Collaboration, *Data-driven determination of the energy scale and resolution of jets reconstructed in the ATLAS calorimeters using dijet and multijet events at $\sqrt{s}$ = 8 TeV*, ATLAS-CONF-2015-017, 2015, URL: https://cds.cern.ch/record/2008678.

[60] ATLAS Collaboration, *Performance of b-jet identification in the ATLAS experiment*, JINST **11** (2016) P04008, arXiv: 1512.01094 [hep-ex].

[61] ATLAS Collaboration, *Optimisation of the ATLAS b-tagging performance for the 2016 LHC Run*, ATL-PHYS-PUB-2016-012, 2016, URL: https://cds.cern.ch/record/2160731.

[62] ATLAS Collaboration, *Commissioning of the ATLAS b-tagging algorithms using $t\bar{t}$ events in early Run 2 data*, ATL-PHYS-PUB-2015-039, 2015, URL: https://cds.cern.ch/record/2047871.

[63] ATLAS Collaboration, *Identification of Boosted, Hadronically Decaying W Bosons and Comparisons with ATLAS Data Taken at $\sqrt{s}$ = 8 TeV*, Eur. Phys. J. C **76** (2016) 154, arXiv: 1510.05821 [hep-ex].

[64] ATLAS Collaboration, *Identification of Boosted, Hadronically-Decaying W and Z Bosons in $\sqrt{s}$ = 13 TeV Monte Carlo Simulations for ATLAS*, ATL-PHYS-PUB-2015-033, 2015, URL: https://cds.cern.ch/record/2041461.

[65] D. Krohn, J. Thaler and L.-T. Wang, *Jet Trimming*, JHEP **02** (2010) 084, arXiv: 0912.1342 [hep-ph].

[66] ATLAS Collaboration, *Jet mass reconstruction with the ATLAS Detector in early Run 2 data*, ATLAS-CONF-2016-035, 2016, URL: https://cds.cern.ch/record/2200211.

[67] A. J. Larkoski, I. Moult and D. Neill, *Power Counting to Better Jet Observables*, JHEP **12** (2014) 009, arXiv: 1409.6298 [hep-ph].

[68] A. J. Larkoski, G. P. Salam and J. Thaler, *Energy Correlation Functions for Jet Substructure*, JHEP **06** (2013) 108, arXiv: 1305.0007 [hep-ph].

[69] ATLAS Collaboration, *Performance of jet substructure techniques for large-R jets in proton-proton collisions at $\sqrt{s}$ = 7 TeV using the ATLAS detector*, JHEP **09** (2013) 076, arXiv: 1306.4945 [hep-ex].

[70] ATLAS Collaboration, *Performance of jet substructure techniques in early $\sqrt{s}$ = 13 TeV pp collisions with the ATLAS detector*, ATLAS-CONF-2015-035, 2015, URL: https://cds.cern.ch/record/2041462.

[71] ATLAS Collaboration, *Flavor Tagging with Track-Jets in Boosted Topologies with the ATLAS Detector*, ATL-PHYS-PUB-2014-013, 2014, URL: https://atlas.web.cern.ch/Atlas/GROUPS/PHYSICS/PUBNOTES/ATL-PHYS-PUB-2014-013.

[72] ATLAS Collaboration, *Boosted Higgs ($\to b\bar{b}$) Boson Identification with the ATLAS Detector at $\sqrt{s}$ = 13 TeV*, ATLAS-CONF-2016-039, 2016, URL: https://cds.cern.ch/record/2206038.

[73] M. Cacciari, G. P. Salam and G. Soyez, *The Catchment Area of Jets*, JHEP **04** (2008) 005, arXiv: 0802.1188 [hep-ph].

[74] M. Aaboud et al., *Electron efficiency measurements with the ATLAS detector using 2012 LHC proton–proton collision data*, Eur. Phys. J. **C77** (2017) 195, arXiv: 1612.01456 [hep-ex].

[75] ATLAS Collaboration, *Electron identification measurements in ATLAS using $\sqrt{s}$ = 13 TeV data with 50 ns bunch spacing*, ATL-PHYS-PUB-2015-041, 2015, URL: https://cds.cern.ch/record/2048202.

[76] ATLAS Collaboration, *Electron and photon energy calibration with the ATLAS detector using LHC Run 1 data*, Eur. Phys. J. C **74** (2014) 3071, arXiv: 1407.5063 [hep-ex].

[77] ATLAS Collaboration, *Muon reconstruction performance of the ATLAS detector in proton–proton collision data at $\sqrt{s}$ = 13 TeV*, Eur. Phys. J. C **76** (2016) 292, arXiv: 1603.05598 [hep-ex].

[78] ATLAS Collaboration, *Performance of algorithms that reconstruct missing transverse momentum in $\sqrt{s}$ = 8 TeV proton–proton collisions in the ATLAS detector*, Eur. Phys. J. C **77** (2017) 241, arXiv: 1609.09324 [hep-ex].

[79] ATLAS Collaboration,
Luminosity determination in pp collisions at $\sqrt{s}$ = 8 TeV using the ATLAS detector at the LHC,
Eur. Phys. J. C **76** (2016) 653, arXiv: 1608.03953 [hep-ex].

[80] G. Cowan, K. Cranmer, E. Gross and O. Vitells,
Asymptotic formulae for likelihood-based tests of new physics, Eur. Phys. J. C **71** (2011) 1554,
arXiv: 1007.1727 [physics.data-an].

[81] A. L. Read, *Presentation of search results: The CL(s) technique*, J. Phys. G **28** (2002) 2693.

[82] WMAP Collaboration, *Nine-Year Wilkinson Microwave Anisotropy Probe (WMAP) Observations: Cosmological Parameter Results*, Astrophys. J. Suppl. **208** (2013) 19,
arXiv: 1212.5226 [astro-ph.CO].

[83] Planck Collaboration, *Planck 2015 results. I. Overview of products and scientific results*,
Astron. Astrophys. **594** (2016) A1, arXiv: 1502.01582 [astro-ph.CO].

[84] Backovic, M. and Kong, K. and Martini, A. and Mattelaer, O. and Mohlabeng, C.,
Direct Detection of Dark Matter with MadDM v.2.0,
Phys. Dark Univ. 9-10 (2015) 37-50 **9-10** (2015) 37, arXiv: 1505.04190 [hep-ph].

[85] E. Gross and O. Vitells, *Trial factors or the look elsewhere effect in high energy physics*,
Eur. Phys. J. C **70** (2010) 525, arXiv: 1005.1891 [physics.data-an].

[86] ATLAS Collaboration, *ATLAS Computing Acknowledgements*, ATL-GEN-PUB-2016-002,
URL: https://cds.cern.ch/record/2202407.